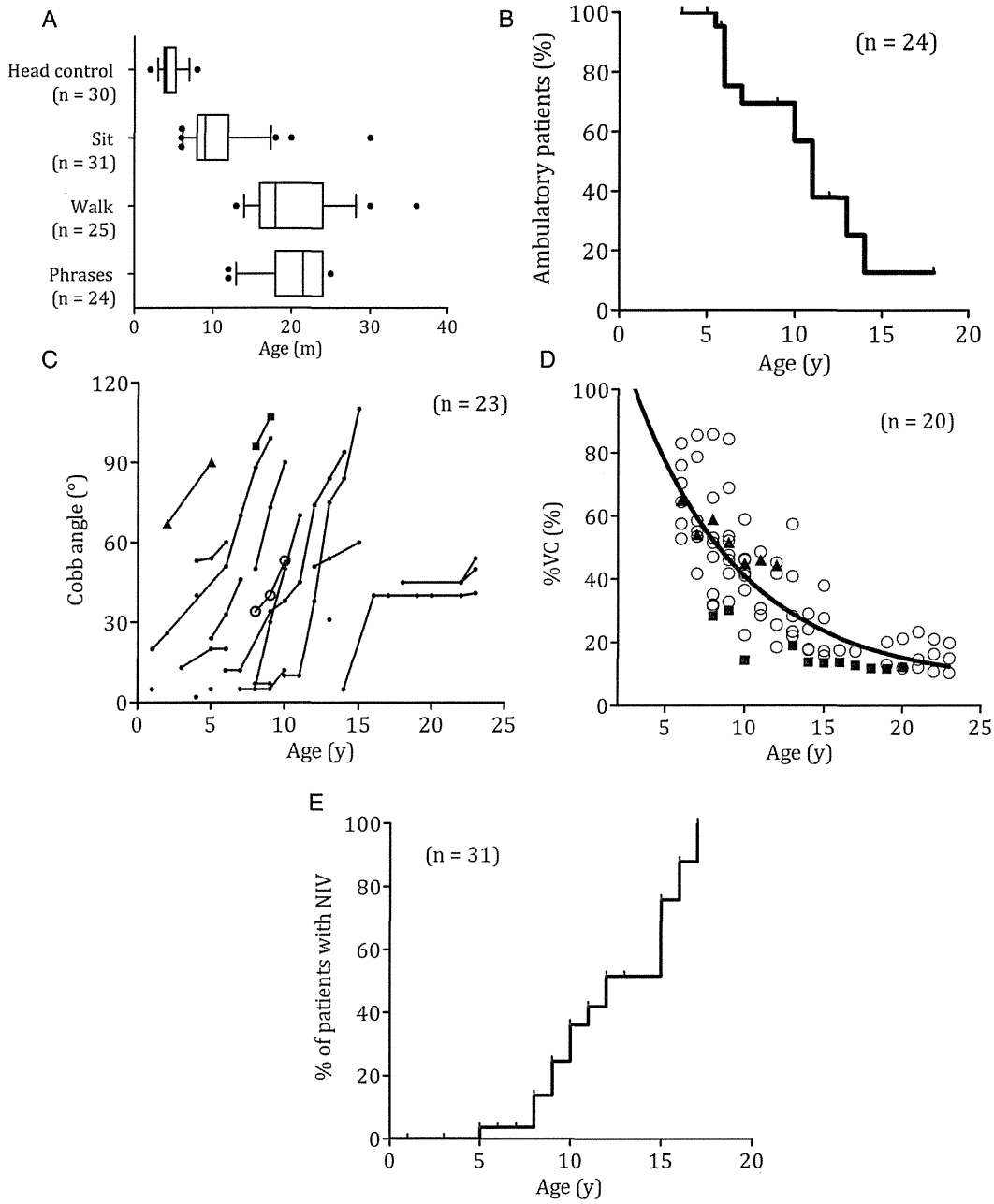

Figure 1 (A) Age ranges at completion of neck control, sit, independent ambulation and phrases. The boxes represent the range from the 25–75th percentile, while the bars span the 10–90th percentile. (B) Kaplan-Meier curve showing deterioration of walking ability in Ullrich congenital muscular dystrophy (n=24). Patients 20 and 30, respectively, become wheelchair-bound at ages 13 years and 6 years. (C) Severity and progression of scoliosis (n=23). Open circles, solid squares and triangles indicate preoperative Cobb angles from Patients 8, 9 and 21 who underwent scoliosis surgery at ages 10 years, 9 years and 5 years, respectively. (D) %Vital capacity (%VC) (n=20). Solid line represents the regression curve (% VC=144.8*exp (−0.146*Age)+7.386, R^2=0.6684). Solid squares and triangles respectively represent values from Patients 9 and 21 who underwent scoliosis surgery at ages 9 years and 5 years. (E) Kaplan-Meier curve showing the percentage of patients with non-invasive ventilation (NIV) (n=31).

clear-cut definition of two major phenotypes.[8 15] According to the clinical classification of early onset COL6-related myopathies, all the patients in our series can be classified into the most severe (early-severe) or moderate-progressive groups.[16 17] The age at loss of ambulation was slightly younger compared with the previous observations (10.7±4.8 years and 10.1 ±4.4 years).[13 17] Interestingly, patients with CD never walked independently or became unable to walk by age 6 years, indicating that CD is most likely to be associated with the more severe phenotype than SSCD. On the other hand, 3 (10.7%) of 28 patients with SSCD did not acquire independent ambulation. Unlike patients with CD, a great heterogeneity in the maximal motor capacity was observed in those with SSCD, ranging from no acquisition of walking ability to retaining ambulation throughout childhood. Four patients with a heterozygous c.850G>A (p.Gly284Arg) mutation in *COL6A1* showed a wide

Table 4 Data of Cobb angle in 23 patients

Pt	COL6 deficiency on IHC	Age at loss of ambulation (years)	Age at assessment (years)																			
			<3	4	5	6	7	8	9	10	11	12	13	14	15	16	17	18	19	20	22	23
1	CD	NW									45											
2	CD	NW					5	5	5	12												
5	CD	6																			45	50
6	SSCD	NW																45			45	54
7	SSCD	NW	26 (2)			51	70	88	99													
8	SSCD	NW						34	40	50												
9	SSCD	6						96	107					80								
10	SSCD	6	13 (3)		20	20																
11	SSCD	7						7	7	10												
12	SSCD	10											31									
13	SSCD	10										51	54		60							
14	SSCD	11						0		10	10	38	75	84	110							
15	SSCD	11				12	12		34	38	45	74	84	94								
16	SSCD	11						5	30	50	70											
17	SSCD	14												5		40	40		40	40	40	41
20	SSCD	W						50	73	90												
21	SSCD	W	67 (2)		90	40																
23	SSCD	W		2																		
24	SSCD	W			5																	
25	SSCD	W		53	54	60																
26	SSCD	W			24	33	46															
32	SSCD	W		40																		
33	SSCD	NW	5 (1)																			

Pts 8, 9 and 21 respectively underwent scoliosis surgery at age 10, 9 and 5 years.
CD, complete deficiency; COL6, collagen VI; IHC, immunohistochemistry; NW, not walk; Pt, patient; SSCD, sarcolemma specific collagen VI deficiency; W, walk.

variety in their ability to walk (table 3). In this study we were not able to confirm recessive mutations and a heterozygous mutation in 2 with CD and 13 with SSCD, respectively. The mutation detection rate (59.4%) was comparable with those reported to be up to 60% in other groups,[15] and those patients without a putative mutation identified may carry deletions or duplications of one or more exons as well as intronic, regulatory mutations.

The onset of scoliosis preceded loss of ambulation in UCMD. This pattern of scoliosis progression was also pointed out by Nadeau *et al*.[13] Development of scoliosis in Duchenne muscular dystrophy, on the other hand, is strongly related to the loss of walking ability.[18] In Duchenne muscular dystrophy, typically, scoliosis is not evident in ambulatory patients and starts after patients become wheelchair dependent. In UCMD, in contrast, scoliosis developed even when patients were still ambulant and is characterised by marked progression from early stage. For the first time, we characterised scoliosis progression in this study. It is noteworthy that scoliosis progresses rapidly, within years, once it starts. The early-onset and rapidly-progressive scoliosis in UCMD may well accelerate physical disability, such as difficulty in sitting, standing and walking, and cause pain. More importantly, scoliosis may well compromise respiratory function by reducing chest wall compliance.

VC declined exponentially with age, with a sharp decrease by age 10 years. Nadeau *et al* showed that forced VC (%predicted) in UCMD declined by 6.6±1.9%/year from age 6 years to 10 years compared with by 0.4±3%/year from age 11 years to 15 years.[13] Although the parameters were different, both studies indicate that UCMD patients develop restrictive respiratory dysfunction rapidly in the first decade of life. This decay in VC might be associated with proximal joint and vertebral contractures together with weakness of the diaphragm. Considering the slower decline of %VC in the youngest patient after surgical correction of scoliosis, earlier surgical intervention to correct spinal deformity may be beneficial for maintaining chest wall compliance, thus preventing progressive respiratory dysfunction. Takaso *et al* successfully performed scoliosis surgery in three patients with UCMD at ages 11 years, 13 years and 17 years, respectively (not enrolled in the present study).[19] However, in these patients, surgery did not prevent deterioration of respiratory function suggesting that at such older ages pulmonary and chest wall compliance might be too severely compromised for patients to benefit from scoliosis surgery, and earlier surgical intervention may be more beneficial. However, further studies are necessary to conclude the efficacy of early scoliosis surgery.

Acknowledgements The authors thank Kanako Goto and Rieko Koyama for their technical assistance.

Contributors TY: designed the study, performed literature search, analysed the data and wrote the manuscript. HK, MO and YKH: supervised all aspects of this study, including the study design, interpretation and manuscript preparation. IN, KS and MS gave valuable comments for the manuscript. IN was involved in analysing and interpreting all the data and also supervised the study design, execution and manuscript preparation.

Funding This study was supported by Intramural Research Grant (23-5) for Neurological and Psychiatric Disorders of NCNP, Research on rare and intractable diseases and Research on Applying Health Technology from the Ministry of Health, Labour and Welfare of Japan.

Competing interests None.

Ethics approval The ethics committee of National Center of Neurology and Psychiatry.

Provenance and peer review Not commissioned; externally peer reviewed.

REFERENCES

1 Okada M, Kawahara G, Noguchi S, *et al*. Primary collagen VI deficiency is the second most common congenital muscular dystrophy in Japan. *Neurology* 2007;69:1035–42.
2 Ullrich O. Kongenitale atonisch-skelerotische Muskeldystrophie ein weiterer Typus der heredodegenerativen Erkrankungen des neuromuskularen systems. *Z Ges Neurol Psychiat* 1930;126:171–201.
3 Nonaka I, Une Y, Ishihara T, *et al*. A clinical and histological study of Ullrich's disease (congenital atonic-sclerotic muscular dystrophy). *Neuropediatrics* 1981;12:197–208.
4 Mercuri E, Yuva Y, Brown SC, *et al*. Collagen VI involvement in Ullrich syndrome: a clinical, genetic, and immunohistochemical study. *Neurology* 2002;58:1354–9.
5 Norwood FL, Harling C, Chinnery PF, *et al*. Prevalence of genetic muscle disease in Northern England: in depth analysis of a muscle clinic population. *Brain* 2009;132:3175–86.
6 Ishikawa H, Sugie K, Murayama K, *et al*. Ullrich disease: collagen VI deficiency: EM suggests a new basis for muscular weakness. *Neurology* 2002;59:920–3.
7 Ishikawa H, Sugie K, Murayama K, *et al*. Ullrich disease due to deficiency of collagen VI in the sarcolemma. *Neurology* 2004;62:620–3.
8 Allamand V, Briñas L, Richard P, *et al*. ColVI myopathies: where do we stand, where do we go? *Skelet Muscle* 2011;1:30–42.
9 Grumati P, Coletto L, Sabatelli P, *et al*. Autophagy is defective in collagen VI muscular dystrophies, and its reactivation rescues myofiber degeneration. *Nat Med* 2010;16:1313–20.
10 ClinicalTrials.gov Identifier: NCT01438788. Clinical Trials.gov Website. http://www.clinicaltrials.gov/ (accessed 4 Dec 2012).
11 Baker NL, Morgelin M, Pace RA, *et al*. Molecular consequences of dominant Bethlem myopathy collagen VI mutations. *Ann Neurol* 2007;62:390–405.
12 Gualandi F, Manzati E, Sabatelli P, *et al*. Antisense-induced messenger depletion corrects a COL6A2 dominant mutation in Ullrich myopathy. *Hum Gene Ther* 2012;23:1313–18.
13 Nadeau A, Kinali M, Main M, *et al*. Natural history of Ullrich congenital muscular dystrophy. *Neurology* 2009;73:25–31.
14 Pepe G, Bertini E, Bonaldo P, *et al*. Bthlem myopathy (BETHLEM) and Ullrich scleroatonic muscular dystrophy: 100th ENMC International Workshop, 23–24 November 2001, Naarden, the Netherlands. *Neuromuscul Disord* 2002;12:984–93.
15 Allamand V, Merlini L, Bushby K. 166th ENMC International Workshop on Collagen type VI- related Myopathies, 22–24 May 2009, Naarden, the Netherlands. *Neuromuscul Disord* 2010;20:346–54.
16 Quijano-Roy S, Allamand V, Riahi N, *et al*. Predictive factors of severity and management of respiratory and orthopaedic complications in 16 Ullrich CMD patients [abstract]. *Neuromuscul Disord* 2007;17:844.
17 Briñas L, Richard P, Quijano-Roy S, *et al*. Early onset collagen VI myopathies: Genetic and clinical correlations. *Ann Neurol* 2010;68:511–20.
18 Mullender MG, Blom NA, De Kleuver M, *et al*. A Dutch guideline for the treatment of scoliosis in neuromuscular disorders. *Scoliosis* 2008;3:14–27.
19 Takaso M, Nakazawa T, Imura T, *et al*. Surgical correction of spinal deformity in patients with congenital muscular dystrophy. *J Orthop Sci* 2010;15:493–501.

Rapidly progressive scoliosis and respiratory deterioration in Ullrich congenital muscular dystrophy

Takahiro Yonekawa, Hirofumi Komaki, Mari Okada, et al.

J Neurol Neurosurg Psychiatry 2013 84: 982-988 originally published online April 9, 2013
doi: 10.1136/jnnp-2012-304710

RESEARCH ARTICLE

Human Mutation

OFFICIAL JOURNAL
HGVS
HUMAN GENOME VARIATION SOCIETY
www.hgvs.org

Mutations in the C-Terminal Domain of ColQ in Endplate Acetylcholinesterase Deficiency Compromise ColQ–MuSK Interaction

Tomohiko Nakata,[1,2] Mikako Ito,[1] Yoshiteru Azuma,[1,2] Kenji Otsuka,[1] Yoichiro Noguchi,[1] Hirofumi Komaki,[3] Akihisa Okumura,[4] Kazuhiro Shiraishi,[5] Akio Masuda,[1] Jun Natsume,[2] Seiji Kojima,[2] and Kinji Ohno[1]*

[1]*Division of Neurogenetics Center for Neurological Diseases and Cancer, Nagoya University Graduate School of Medicine, Nagoya, Japan;* [2]*Department of Pediatrics Nagoya University Graduate School of Medicine, Nagoya, Japan;* [3]*Department of Child Neurology National Center Hospital, National Center of Neurology and Psychiatry (NCNP), Tokyo, Japan;* [4]*Department of Pediatrics Juntendo University Faculty of Medicine, Tokyo, Japan;* [5]*Department of Pediatrics Utano National Hospital, Kyoto, Japan*

Communicated by Lars Bertram

Received 19 January 2013; accepted revised manuscript 19 March 2013.
Published online 29 March 2013 in Wiley Online Library (www.wiley.com/humanmutation). DOI: 10.1002/humu.22325

ABSTRACT: Acetylcholinesterase (AChE) at the neuromuscular junction (NMJ) is mostly composed of an asymmetric form in which three tetramers of catalytic AChE subunits are linked to a triple helical collagen Q (ColQ). Mutations in *COLQ* cause endplate AChE deficiency. We report three patients with endplate AChE deficiency with five recessive *COLQ* mutations. Sedimentation profiles showed that p.Val322Asp and p.Arg227X, but not p.Cys444Tyr, p.Asp447His, or p.Arg452Cys, inhibit formation of triple helical ColQ. In vitro overlay of mutant ColQ-tailed AChE on muscle sections of *Colq*$^{-/-}$ mice revealed that p.Cys444Tyr, p.Asp447His, and p.Arg452Cys in the C-terminal domain (CTD) abrogate anchoring ColQ-tailed AChE to the NMJ. In vitro plate-binding assay similarly demonstrated that the three mutants inhibit binding of ColQ-tailed AChE to MuSK. We also confirmed the pathogenicity of p.Asp447His by treating *Colq*$^{-/-}$ mice with adeno-associated virus serotype 8 carrying mutant *COLQ*-p.Asp447His. The treated mice showed no improvement in motor functions and no anchoring of ColQ-tailed AChE at the NMJ. Electroporation of mutant *COLQ* harboring p.Cys444Tyr, p.Asp447His, and p.Arg452Cys into anterior tibial muscles of *Colq*$^{-/-}$ mice similarly failed to anchor ColQ-tailed AChE at the NMJ. We proved that the missense mutations in ColQ–CTD cause endplate AChE deficiency by compromising ColQ–MuSK interaction at the NMJ.
Hum Mutat 34:997–1004, 2013. © 2013 Wiley Periodicals, Inc.

KEY WORDS: COLQ; collagen Q; neuromuscular; acetylcholinesterase; myasthenic syndromes

Introduction

Congenital myasthenic syndromes (CMS) are clinically and genetically heterogeneous inherited disorders characterized by neuromuscular transmission defect caused by mutations affecting proteins expressed at the neuromuscular junction (NMJ) [Engel et al., 2003]. The synaptic type of CMS is caused by the absence of the asymmetric form of acetylcholinesterase (AChE) from the endplate [Engel et al., 1977]. Endplate AChE deficiency is characterized by generalized muscle weakness, fatigue, scoliosis, minor facial abnormalities, and episodes of respiratory distress [Mihaylova et al., 2008]. In the absence of AChE, the duration of the endplate currents are prolonged, so that it outlasts the refractory period of the skeletal muscle sodium channel, which in turn evokes repetitive compound muscle action potentials (CMAPs). Four mechanisms lead to defective neuromuscular signal transmission in endplate AChE deficiency [Engel et al., 1977; Ohno et al., 1998]. First, the prolonged endplate currents lead to overload of Ca^{2+} ions at the postsynaptic sarcoplasm, which causes endplate myopathy with loss of acetylcholine receptor (AChR). Second, excessive ACh at the synaptic space causes desensitization of AChR. Third, repeated opening of AChR causes staircase summation of endplate potentials, which depolarizes the resting membrane potential and makes the muscle sodium channel irresponsive to an endplate potential. Fourth, lack of ColQ at the NMJ diminishes the amount of membrane-bound MuSK and reduces phosphorylation of the AChR β subunit, which compromises AChR clustering [Sigoillot et al., 2010]. Lack of effects of cholinesterase inhibitors, or even worsening of the symptoms with them, in patients with endplate AChE deficiency suggests that lack of AChE rather than lack of AChR is a key underlying mechanism leading to myasthenic symptoms.

Endplate AChE deficiency is not caused by mutations in the *ACHE* gene (NM_000665.3; MIM #100740) encoding the catalytic subunit but is caused by recessive mutations in the *COLQ* gene (NM_005677.3; MIM #603033) encoding the collagenic tail subunit [Ohno et al., 1998]. There are two major types of AChE in the skeletal muscle: (1) globular forms consisting of monomers (G_1), dimmers (G_2), or tetramers (G_4) of the T isoform of the catalytic subunit ($AChE_T$, NP_000656.1), and (2) asymmetric forms consisting of one, two, or three homotetramers (A_4, A_8 and A_{12}, respectively) of $AChE_T$ attached to a triple-stranded collagenic tail (ColQ) [Massoulie, 2002], which are hereafter called ColQ-tailed

Additional Supporting Information may be found in the online version of this article.

*Correspondence to: Kinji Ohno, Division of Neurogenetics, Center for Neurological Disease and Cancer, Nagoya University Graduate School of Medicine, 65 Tsurumai, Showa-ku, Nagoya 466-8550, Japan. E-mail: ohnok@med.nagoya-u.ac.jp

Contract grant sponsors: Ministry of Education, Culture, Sports, Science, and Technology of Japan, and the Ministry of Health, Labor, and Welfare of Japan.

AChE species. ColQ carries three domains: (1) an N-terminal proline-rich attachment domain that organizes the catalytic AChE subunits into a tetramer, (2) a collagen domain that forms a triple helix and contains heparin-binding domains, and (3) a C-terminal domain (CTD) enriched in charged residues and cysteines.

In previous studies, *COLQ* mutations were divided into- four classes according to their positions in ColQ and their effects on the expression of AChE species in COS cells: (1) N-terminal mutations that prevent association of $AChE_T$ with ColQ, (2) truncation mutations in the collagen domain that prevent the formation of ColQ-tailed AChE, (3) CTD missense mutations that prevent triple helical formation of ColQ, and (4) CTD mutations that do not abolish formation of ColQ-tailed AChE but affect anchoring of ColQ at the NMJ [Ohno et al., 2000]. We previously reported that p.Asp342Glu, p.Arg410Pro, and p.Arg410Glu, but not p.Cys444Tyr, at the CTD of ColQ compromise anchoring ColQ-tailed AChE to heterologous frog muscle sections [Kimbell et al., 2004]. We, however, did not show how the mutations affect anchoring of ColQ to the synaptic basal lamina. We also failed to prove pathogenicity of p.Cys444Tyr in the heterologous anchoring experiment. Two binding partners for anchoring ColQ-tailed AChE at the synaptic basal lamina have been reported to date: (1) the heparan sulfate proteoglycans such as perlecan, which bind to two heparan sulfate proteoglycan binding domains in the ColQ collagen domain [Arikawa-Hirasawa et al., 2002], and (2) the extracellular domain of MuSK, a muscle-specific receptor tyrosine kinase, on the postsynaptic membrane, which binds to the CTD of ColQ [Cartaud et al., 2004]. We recently demonstrated that anti-MuSK autoantibodies in patients with myasthenia gravis block binding of ColQ to MuSK [Kawakami et al., 2011]. We also reported that intravenous or intramuscular administration of adeno-associated virus serotype 8 (AAV8) carrying human *COLQ* efficiently anchors ColQ-tailed AChE at the NMJ [Ito et al., 2012]. We proved that ColQ-tailed AChE moves from one muscle to another and anchors to the synaptic basal lamina by exploiting the proprietary binding affinity for synaptic basal lamina, which we named the protein-anchoring therapy.

We here report three patients with AChE deficiency harboring *COLQ* mutations in the collagen domain and CTD. We examined the effects of the CTD mutations on interaction between ColQ and MuSK by in vitro and in vivo assays and found that the CTD mutations impair this interaction.

Materials and Methods

Patients

All human studies were performed under approvals of the institutional review boards of Nagoya University Graduate School of Medicine, National Center of Neurology and Psychiatry, Juntendo University Faculty of Medicine, and Utano National Hospital. Three patients participated in the study after appropriate informed consents were given. A mutation analysis had been done when they were 7, 12, and 19 years of age, respectively. All had respiratory distress or poor sucking at birth, slight delay in walking, fatigability since early childhood, normal intelligence, no anti-AChR and anti-MuSK antibodies, a decremental electromyographic response, repetitive CMAP to a single nerve stimulus, and no response to anticholinesterase medications (Table 1).

Mutation Analysis

Genomic DNA was isolated from blood with QIAamp Blood Mini Kit (Qiagen, Hilden, Germany). Poor response to anticholinesterases suggested endplate AChE deficiency and slow channel syndrome. We thus directly sequenced 17 constitutive *COLQ* exons and their flanking regions with CEQ8000 sequencer (Beckman Coulter, Brea, CA). Names of all mutations were checked using Mutalyzer (http://www.lovd.nl/mutalyzer/). Identified mutations were submitted to an LSDB for the *COLQ* gene (http://www.lovd.nl/COLQ). As mutations were identified in *COLQ* in all the patients, we did not go into sequencing of *CHRNA1* (NM_00079.3; MIM #100690), *CHRNB1* (NM_009601.4; MIM #100710), *CHRND* (NM_021600.2; MIM #100720), and *CHRNE* (NM_000080.3; MIM #100725) encoding the AChR α, β, δ, and ε subunits, respectively.

Construction of Expression Vectors

Human $ACHE_T$, *COLQ* cDNAs, and LacZ were cloned and introduced into a cytomegalovirus-based mammalian expression vector pTargeT (Promega, Madison, WI) [Ohno et al., 1998]. Each mutation was introduced into *COLQ* cDNA using the QuikChange site-directed mutagenesis kit (Stratagene). The extracellular domain (aa 1–393) of human *MUSK* (NM_001166280.1; MIM #601296) cDNA (Open Biosystems/Thermo Scientific, Waltham, MA) was cloned into a mammalian expression vector pAPtag-5 (GenHunter, Nashville, TN) at the *Nbe*I and *Xbo*I sites upstream of a myc epitope [Kawakami et al., 2011].

Transfection and AChE Extraction

Wild-type or mutant pTargeT-*COLQ* was transfected into COS7 cells along with pTargeT-$ACHE_T$ in a 10-cm dish using X-tremeGENE 9 DNA Transfection Reagent (Roche Diagnostics, Indianapolis, IN). Cells were incubated at 37°C for 48 hr and scraped from dish in Tris–HCl buffer (50 mM Tris–HCl [pH 7.0], 0.5% Triton X-100, 0.2 mM EDTA, 2 μg/ml leupeptin, 1 μg/ml pepstatin, and 0.1 μmol/ml benzamidine) containing 1 M NaCl. The extract was vortexed in a 1.5-ml tube and centrifuged at 14,000*g* for 5 min, and the supernatant was obtained.

Sedimentation Analysis

A sedimentation analysis was performed as previously described [Ohno et al., 1998]. The AChE-containing supernatant was applied on a 5%–20% sucrose density gradient, which was made in Tris–HCl buffer along with β-galactosidase (16.1 S) and alkaline phosphatase (6.1 S) as internal sedimentation standards. Centrifugation was performed in a Beckman SW41Ti rotor at 4°C for 21 hr at 178300*g*. The collected fractions were assayed for AChE activities using the Ellman method [Ellman et al., 1961] and determined the absorbance at 420 nm using a Sunrise Absorbance Reader (Tecan, Männedorf, Switzerland).

Isolation of ColQ-Tailed AChE on a Heparin–Agarose Column

For isolation of ColQ-tailed AChE, the extract was diluted in Tris–HCl buffer containing 0.2 M NaCl and loaded onto a HiTrap Heparin HP column (GE Healthcare, Buckinghamshire, UK). We washed the column with five volumes of Tris–HCl buffer containing 0.2 M NaCl, and eluted ColQ-tailed AChE with Tris–HCl buffer containing 1 M NaCl. We concentrated the eluate with an Amicon Ultra-4 Centrifugal Filter (50K) (Millipore, Billerica, MA) [Kawakami et al., 2011; Kimbell et al., 2004].

Table 1. Clinical Features and Mutations

Pt.	Sex	Age	Onset	Walking	Noc. NIV	Edrophonium i.v.	RNS	rCMAP	Exon	Nucleotide change	Amino-acid change
1	M	19 y	Birth	19 m	12 y	No change	−52%	+	11	c.679C>T	p.Arg227X
									14	c.965T>A	p.Val322Asp
2	M	12 y	Birth	24 m	11 y	Respiratory distress	−32%	+	17	c.1339G>C[a]	p.Asp447His[a]
3	M	7 y	3 y	18 m	Not used	Improved	−79%	+	17	c.1331G>A	p.Cys444Tyr
									17	c.1354C>T	p.Arg452Cys

[a]Homozygous mutation.
Exon numbers are according to GenBank Accession NM_005677.3. Mutations are numbered according to NM_005677.3 (cDNA) and NP_005668.2 (protein). cDNA number +1 corresponds to the A of the ATG translation initiation codon.
Pt., patient; Noc. NIV, nocturnal noninvasive ventilation; RNS, repetitive nerve stimulation at 3 Hz of ulnar or accessory nerves; rCMAP, repetitive compound muscle action potential; m, months; y, years.

Transplantation of ColQ-tailed AChE to NMJs of *Colq*$^{-/-}$ Mice

We obtained approvals of the *Colq*$^{-/-}$ mice[Feng et al., 1999] studies by the Animal Care and Use Committee of the Nagoya University. We prepared 10-μm-thick sections of quadriceps muscles of *Colq*$^{-/-}$ mice with a Leica CW3050–4 cryostat at −20°C, and stored at −80°C until used. The muscle sections were fixed in acetone for 15 min. The stock solutions of ColQ-tailed AChE were diluted in Tris–HCl buffer containing 1 M NaCl and 5 mg/ml each of bovine serum albumin, chicken ovalbumin, and gelatin to give an Ellman unit equivalent to 1–2 ng of Torpedo AChE (Sigma, St. Louis, MO), and the NaCl concentration was adjusted to 0.5 M. To adjust the ionic strength of the solution, we added 50 mM Tris–HCl buffer stepwise over a period of 3 hr to 0.3 M NaCl. The slides were placed in a humidified chamber and incubated overnight at room temperature [Kimbell et al., 2004; Rotundo et al., 1997].

Immunofluorescence

For preparation of immunofluorescence, muscle sections were blocked with 5% horse serum in phosphate-buffered saline for 20 min. We detected ColQ-tailed AChE by anti-ColQ antibody [Ito et al., 2012] and anti rabbit-FITC secondary antibody at 1:100 (Vector Lab., Burlingame, CA), along with 2.5 μg/ml Alexa-594-conjugated α-bungarotoxin (Sigma) for visualizing AChR. Signals of ColQ and AChR were examined with fluorescent microscope, BX60 (Olympus, Tokyo, Japan). We analyzed more than 10 muscle sections for each experiment and representative images are indicated in the figures.

Preparation of the Extracellular Domain of MuSK

pAPtag-5 carrying hMuSKect-myc was transfected into HEK293 cells in a 10-cm dish using the calcium phosphate method. The hMuSKect-myc was purified with the c-myc-Tagged Protein Mild Purification Kit version 2 (MBL, Nagoya, Japan) [Kawakami et al., 2011].

In Vitro Plate-Binding assay for ColQ–MuSK Interaction

The Maxi-Sorp Immuno Plate (Nunc/Thermo Scientific) was coated with purified hMuSKect-myc at 4°C overnight and then blocked with phosphate-buffered saline containing 1% bovine serum albumin at room temperature for 1 hr. We incubated an equal Ellman unit of wild-type or mutant ColQ-tailed AChE at 4°C for 4 hr and then quantified the bound ColQ-tailed AChE by the Ellman method. Each time before we moved to the next step, we washed the plate three times with phosphate-buffered saline [Kawakami et al., 2011].

In Vivo Electroporation of pTarget-*COLQ*

The tibialis anterior muscles of *Colq*$^{-/-}$ mice were injected with 50 μg each of pTargeT-*COLQ* and pTargeT-LacZ plasmids. In vivo transfection was performed using an in vivo electroporator (CUY21EDIT; BEX Co., Ltd., Tokyo, Japan). A pair of electrode needles was inserted into the muscle in the longitudinal direction to a depth of 4 mm to encompass the plasmid-injected site. Pulses of 50 V and 25-msec were administered every 1 sec three times in forward polarity and three more times in the opposite polarity [Aihara and Miyazaki, 1998]. Seven days after the electroporation, mice were sacrificed and tibialis anterior muscles were analyzed.

AAV8-Mediated Expression of Mutant ColQ in *Colq*$^{-/-}$ Mice

We prepared wild-type and mutant pAAV8-*COLQ* and intravenously administered them to *Colq*$^{-/-}$ mice as described previously [Ito et al., 2012]. We inserted the wild-type human *COLQ* or mutant human *COLQ* harboring p.Asp447His into downstream of a CMV promoter in the pAAV-MCS vector using the AAV Helper-Free system (Stratagene). We employed AAV serotype 8 that can efficiently infect skeletal muscles. We injected 2×10^{12} vector genomes of wild-type or mutant pAAV-*COLQ* to the tail vein of 4-week-old male *Colq*$^{-/-}$ mice. Similar copies of wild-type pAAV8-*COLQ* and mutant pAAV8-*COLQ*-p.Asp447His genomes were transduced into muscle cells with a mean ratio of 1.07 (mutant transgene/wild-type transgene, $n = 3$). We quantified motor functions up to 4 weeks after injection. Muscle weakness and fatigability were measured with a rotarod apparatus (Ugo Basile). Mice were allowed to take a rest for 1 hr between each rotarod task and an average of three measurements was taken. Spontaneous running-wheel activities were used to quantify voluntary exercises. Each mouse was placed in a standard cage equipped with a counter-equipped running wheel (diameter, 14.7 cm; width, 5.2 cm; Ohara Medical Corp., Tokyo, Japan). The running distances were recorded every 24 hr. At 6 weeks after injection, mice were sacrificed and sections of skeletal muscles were stained for AChR and ColQ to visualize the transduced ColQ-tailed AChE as described above.

Results

Mutation Analysis

On the basis of combined clinical and electrophysiological features such as early age of onset, negative response to cholinesterase inhibitors, respiratory insufficiency, and repetitive muscle response [Abicht et al., 2012; Engel, 2012], we first sequenced *COLQ* and identified that each patient carried two mutant *COLQ* alleles. Patient 1 had heterozygous [c.679C>T, p.Arg227X] +

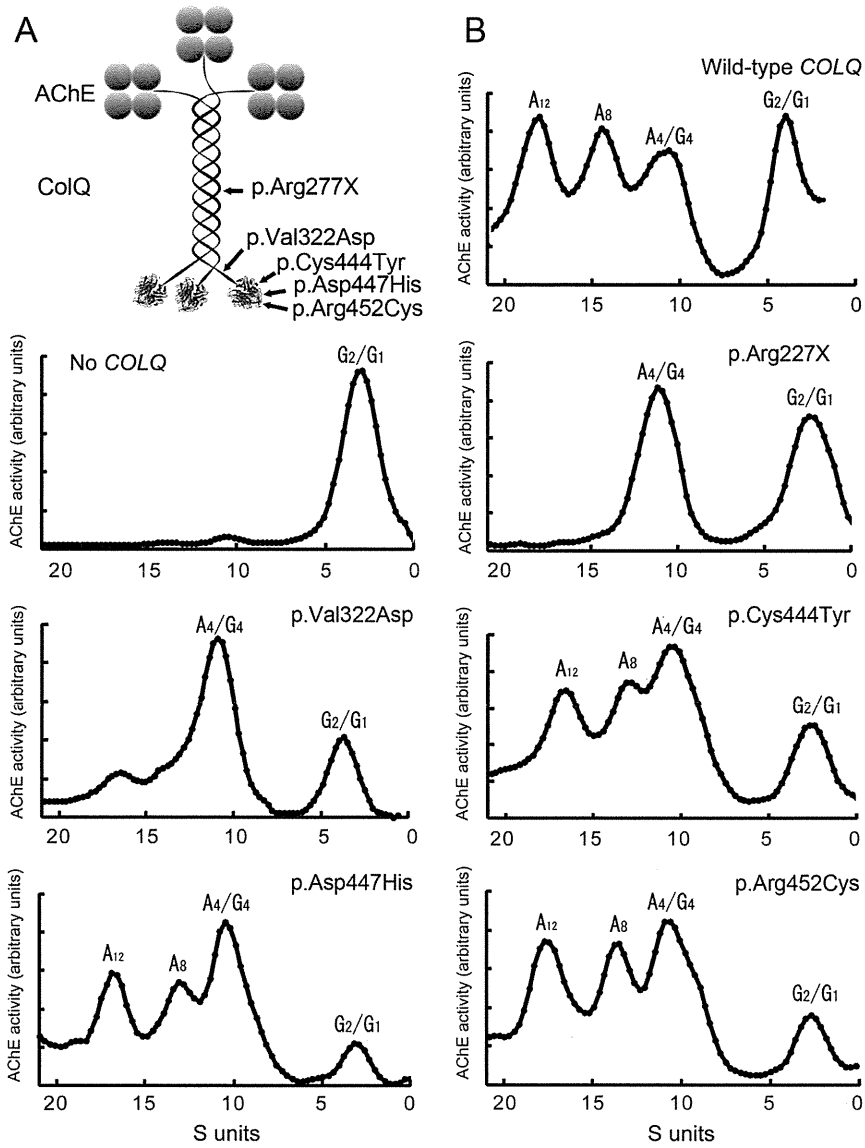

Figure 1. **A:** Schematic presentation of positions of the identified mutations in ColQ. **B:** Sedimentation profiles of AChE species extracted from COS cells transfected with wild-type *ACHE*$_T$ cDNA and indicated *COLQ* cDNA. p.Arg227X is in the collagen domain, the other four missense mutations are in the C-terminal domain. p.Val322Asp has a small ~16-S peak (A_{12} species), whereas the other missense mutations in the C-terminal region do not abolish formation of asymmetric AChE species. G_1, G_2, and G_4, globular forms; A_4, A_8, and A_{12}, asymmetric forms.

[c.965T>A, p.Val322Asp] mutations. Patient 2 was heterozygous for [c.1331G>A, p.Cys444Tyr] + [c.1354C>T, p.Arg452 Cys]. Patient 3 had a homozygous [c.1339G>C, p.Asp447His] mutation (Fig. 1A, Table 1, Supp. Fig. S1). We traced the mutations in the parents of patients 1 and 3, and found that the mutation on each allele was inherited from unaffected parents. In patient 2, we confirmed heterozygosity by cloning each allele of exon 17 and sequenced them. Among the five mutations, only c.1331G>A, p.Cys444Tyr was previously identified in another Japanese patient [Ohno et al., 2000], but its pathogenicity remained elusive [Kimbell et al., 2004]. The other four mutations were novel. All the amino acids at mutated codons were conserved across species [Ohno et al., 1998].

Sedimentation Profiles of Mutations

Four missense mutations were in CTD and the nonsense p.Arg227X was in the collagen domain. We first examined the effects of the mutations on formation of asymmetric ColQ-tailed AChE species in COS cells. The p.Arg227X mutation that truncates ColQ in its collagen domain did not produce normal A_{12} species of ColQ-tailed AChE, as has been observed in other truncation mutations in the collagen domain [Ohno et al., 1998; 2000]. The p.Val322Asp mutation close to the N-terminal end of CTD similarly failed to produce A_{12} species. By contrast, the other three CTD mutations (p.Cys444Tyr, p.Asp447His, and p.Arg452Cys) produced

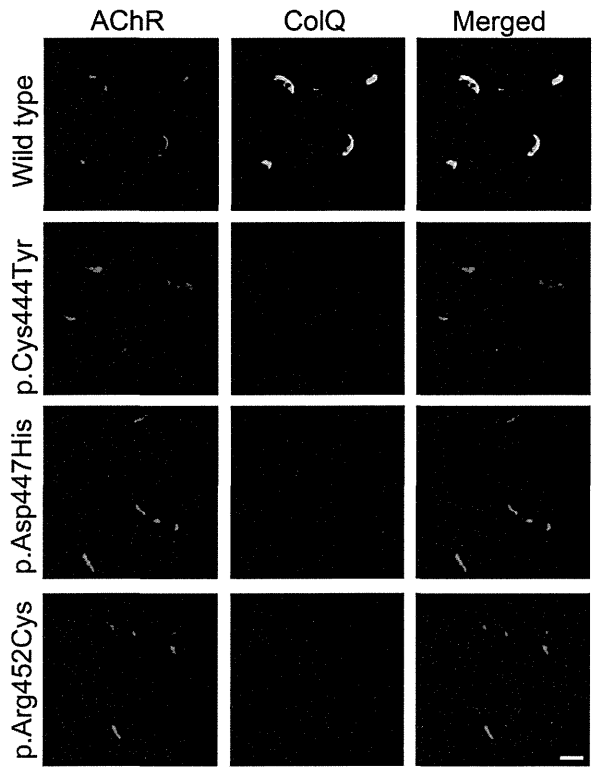

Figure 2. In vitro overlay assays. Plasmid encoding the indicated CTD mutations of human ColQ were cotransfected into COS cells together with a plasmid encoding the wild-type human $AChE_T$ catalytic subunit. The A_{12} AChE expressed in COS cells was isolated and overlaid on a 10-μm quadriceps muscle section of *Colq*$^{-/-}$ mice. ColQ-tailed AChE molecules harboring the indicated mutations do not colocalize with AChRs. ColQ is stained with anti-ColQ antibody and AChR with Alexa594-labeled α-bungarotoxin. Scale bar = 20 μm.

normal or slightly reduced peaks of asymmetric A_4, A_8, and A_{12} species compared to the wild-type (Fig. 1B).

Overlay of CTD Mutants to the NMJ of *Colq*$^{-/-}$ Mice

We overlaid the purified recombinant human ColQ-tailed AChE protein complex on a section of skeletal muscle of *Colq*$^{-/-}$ mice. Wild-type ColQ-tailed AChE colocalized with AChR at the NMJs, whereas ColQ-tailed AChE with p.Cys444Tyr, p.Asp447His, and p.Arg452Cys mutations failed to colocalize with AChR (Fig. 2). This assay showed that these CTD mutations impair anchoring of ColQ at the vertebrate NMJs.

In Vitro Plate-Binding Assay for ColQ–MuSK Interaction

As the synaptic anchorage of AChE by ColQ is partly dependent on the association of ColQ with MuSK [Cartaud et al., 2004], we next examined whether the CTD mutations had an effect on the interaction of human ColQ and human MuSK using an in vitro plate-binding assay. We coated the plate with purified hMuSKect-myc, and added a fixed amount of the purified recombinant human ColQ-tailed AChE protein complex. The bound AChE was quantified by the Ellman method. AChE activities of the CTD mutants carrying p.Cys444Tyr, p.Asp447His, and p.Arg452Cys were significantly lower than that of wild-type CTD (Fig. 3). These results showed that impaired anchoring of the mutant ColQ-tailed AChE was due to the lack of interaction between ColQ and MuSK.

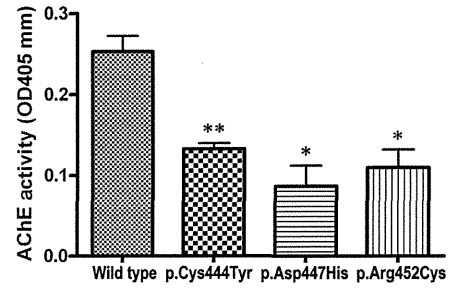

Figure 3. In vitro plate-binding assays. The extracellular domain of human MuSK (hMuSKect-myc) was coated on a 96-well plate. Purified recombinant ColQ-tailed AChE was overlaid on the plate. Bound ColQ-tailed AChE was quantified by AChE activity. $^*P < 0.05$, $^{**}P < 0.01$ by Student's *t*-test.

In Vivo Electroporation of *COLQ* with CTD Mutations into the Muscles of *Colq*$^{-/-}$ Mice

To confirm whether the three CTD mutants indeed impair anchoring of ColQ-tailed AChE to the NMJ in vivo, we electroporated wild-type and mutant pTargeT-*COLQ* constructs to tibialis anterior muscles of *Colq*$^{-/-}$ mice. We first confirmed that the pTargeT-LacZ plasmid is efficiently transduced into muscle fibers (Fig. 4A). ColQ-tailed AChE harboring p.Cys444Tyr, p.Asp447His, and p.Arg452Cys in CTD did not anchor to the NMJs of *Colq*$^{-/-}$ mice (Fig. 4), although real-time RT-PCR revealed similar expression levels of the wild-type and mutant *COLQ* mRNAs (ranges of *COLQ*/*Gapdh* mRNAs = 0.03 to 0.11 for wild-type and three mutants). These studies revealed that the three mutant ColQ molecules were incompetent for anchoring to the NMJ in vivo.

AAV8-Mediated Expression of Mutant ColQ in *Colq*$^{-/-}$ Mice

We previously reported the protein-anchoring therapy for *Colq*$^{-/-}$ mice, in which ColQ-tailed AChE is moved to and anchored to remote NMJs using its proprietary binding affinities for perlecan and MuSK [Ito et al., 2012]. To directly prove that the CTD mutations compromise anchoring of ColQ to the NMJ in a model animal, we intravenously administered wild-type and p.Asp447His-mutant AAV8-*COLQ* to *Colq*$^{-/-}$ mice, and analyzed motor functions and histological localization of ColQ. Motor functions evaluated by the dwell time on a rotarod (Fig. 5A) and by voluntary movements (Fig. 5B) were prominently improved in *Colq*$^{-/-}$ mice treated with wild-type *COLQ* but not with p.Asp447His-*COLQ*. Histological studies similarly showed that ColQ was colocalized to AChR in *Colq*$^{-/-}$ mice treated with AAV-wild-type *COLQ* but not with AAV-p.Asp447His-*COLQ* (Fig. 5C).

Discussion

CMSs have a variety of causes that lead to defects in the NMJ signal transmission. Elucidation of the molecular pathomechanisms is essential to develop and provide a specific treatment for CMS patients. Ephedrine and albuterol are effective for patients with

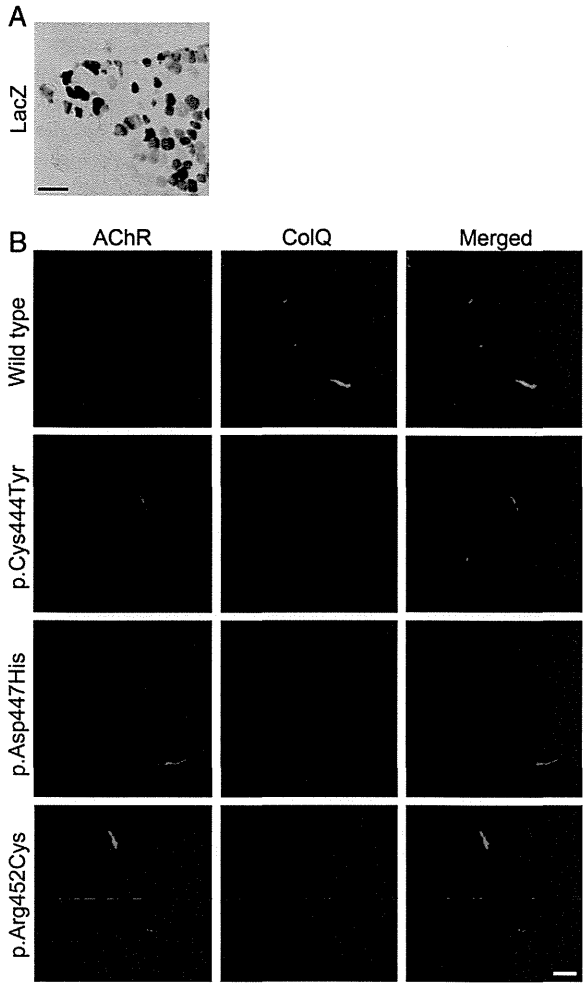

Figure 4. In vivo electroporation. **A:** Histochemical staining for β-galactosidase activity in the muscle after gene transfer of pTargeT-lacZ with electroporation. The transverse section of the muscle was stained with X-gal. **B:** Immunocytochemistry using serial muscle sections showed that ColQ-tailed AChE molecules harboring p.Val322Asp, p.Asp447His, p.Cys444Tyr, and p.Arg452Cys in ColQ, do not colocalize with AChRs in tibialis anterior muscles of *Colq*$^{-/-}$ mice. ColQ is stained with anti-ColQ antibody and AChR with Alexa594-labeled α-bungarotoxin. Scale bar = 100 μm (**A**) and 20 μm (**B**).

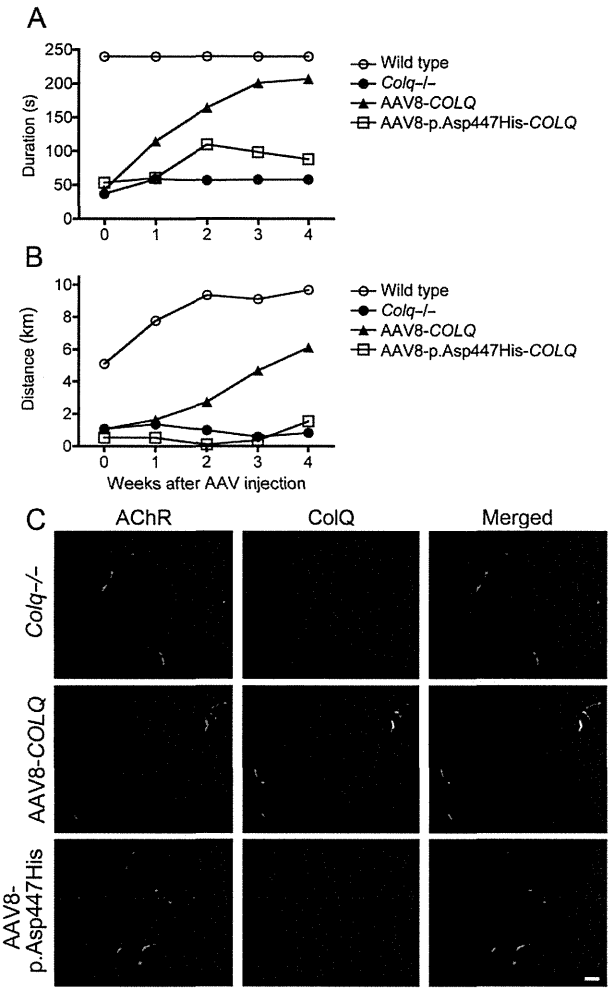

Figure 5. AAV8-mediated expression of mutant ColQ in *Colq*$^{-/-}$ mice. **A**: Temporal profiles of dwell times on a rotarod that linearly accelerated from 0 to 40 rpm in 240 sec. **B**: Voluntary movements per day were quantified with a counter-equipped running wheel. **C**: Visualization of ColQ-AChE and AChR on the section of skeletal muscle using anti-ColQ antibody and α-bungarotoxin, respectively. AAV8-*COLQ*-p.Asp447His failed to anchor ColQ-tailed AChE to the NMJ. Scale bar = 20 μm.

endplate AChE deficiency harboring *COLQ* mutations [Chan et al., 2012; Engel et al., 2010]. Cholinesterase inhibitors cannot improve neuromuscular transmission and often worsen myasthenic symptoms and respiratory conditions. Therefore, an early genetic diagnosis is important for the patients. Clinical features of the three patients prompted us to search for mutations in *COLQ*, and indeed we detected five *COLQ* mutations. Four of them are novel and p.Cys444Tyr has been previously reported in another Japanese patient [Ohno et al., 2000]. It is interesting to note that the five mutations are unique to Japanese patients, which suggests that all the mutations have recently arisen in the patients' families and are unlikely to be founder mutations.

In 1998, we cloned human *COLQ* cDNA, identified its genomic structure, and detected *COLQ* mutations in patients with endplate AChE deficiency [Ohno et al., 1998]. We also proved that mutations in the collagen domain impair formation of ColQ-tailed AChE [Ohno et al., 1998]. We later reported four classes of *COLQ* mutations as stated in the introduction, and proved pathogenicity in three classes but not in a class comprising CTD mutations [Ohno et al., 1999; 2000]. We next proved pathogenicity of five mutations (p.Arg315X, p.Asp342Glu, p.Gln371X, p.Arg410Gln, and p.Arg410Pro) in CTD using the heterologous overlay of human ColQ-tailed AChE to the frog muscles, but another mutation, p.Cys444Tyr, had no effect on anchoring of ColQ to the frog NMJ [Kimbell et al., 2004]. To summarize, we have reported 23 *COLQ* mutations and have succeeded in proving the pathogenicity in 22 mutations [Kimbell et al., 2004; Ohno et al., 1998; 1999; 2000; Shapira et al., 2002]. p.Cys444Tyr in CTD has thus been the only mutation that we failed to prove why the patient was deficient for AChE. Donger et al. (1998) reported p.Tyr430Ser in CTD in a patient with endplate AChE deficiency, but the sedimentation analysis yielded normal asymmetric species of AChE. The p.Tyr430Ser mutation was later employed to prove that CTD binds to MuSK by immunoprecipitation experiments [Cartaud et al., 2004]. Four

additional mutations (p.Arg341Gly, p.Cys386Ser, p.Cys417Tyr, and p.Thr441Ala) in CTD have been reported by others but none have been functionally analyzed [Mihaylova et al., 2008; Muller et al., 2004].

In the present study, we found four missense mutations (p.Val322Asp, p.Asp447His, p.Cys444Tyr, and p.Arg452Cys) in CTD and one truncation mutation (p.Arg227X) in the collagen domain in three patients with endplate AChE deficiency. Three mutations (p.Val322Asp, p.Asp447His, and p.Arg452Cys) in CTD have not been functionally characterized and one was p.Cys444Tyr, for which the pathogenicity remained elusive. We characterized the functional consequences of these mutations.

The analysis of sedimentation profiles revealed that p.Arg227X and p.Val322Asp abolish formation of normal asymmetric A_{12} species of AChE. p.Val322Asp is the only mutation that affects formation of A_{12} and is the only mutation that introduces a negatively charged residue in CTD. We previously reported that 1082delC in CTD introduces 64 hydrophobic missense residues after the frameshift, which prevents triple helix formation [Ohno et al., 2000]. CTD is enriched with prolines, cysteines, and charged residues. The hydrophobicity profile is likely to be essential in CTD. p.Val322Asp introduces a hydrophilic aspartate residue, and disrupts a hydrophobic cluster close to the N-terminal end of CTD (Supp. Fig. S2A). Prediction of a secondary structure similarly demonstrates shortening of a β-sheet and de novo insertion of a turn before an α-helix (Supp. Fig. S2B). We do not observe these gross alterations in predicted structures with p.Cys444Tyr, p.Asp447His, and p.Arg452Cys (Supp. Fig. S2). p.Val322Asp is thus likely to compromise the tertiary structure of CTD and leads to defective triple helix formation.

The analysis of sedimentation profiles showed that the other CTD mutations, p.Cys444Tyr, p.Asp447His, and p.Arg452Cys, generated normal asymmetric A_{12} species of AChE. We next examined the anchoring competence of these mutations. We had previously employed frog muscles to analyze anchoring incompetence of CTD mutations, but failed to prove it for p.Cys444Tyr [Kimbell et al., 2004]. We thus used the vertebrate NMJs of *Colq*$^{-/-}$ mice, and proved that all three mutations are not able to anchor to the mouse NMJ. Anchoring competence of p.Cys444Tyr to frog NMJs but not to mouse NMJs suggests that p.Cys444Tyr does not grossly change the conformation of CTD and is likely to be a mild mutation. Indeed, the onset of patient 3 carrying p.Cys444Tyr was at the age of 3 years, and the patient started walking at 18 months, which are the mildest among the three currently analyzed patients.

To further dissect the underlying molecular bases of anchoring incompetence of p.Cys444Tyr, p.Asp447His, and p.Arg452Cys, we quantified the ColQ–MuSK interaction by the in vitro plate-binding assay, which enabled us to estimate the binding affinities of these two molecules. The three missense mutations decreased the activities of ColQ-tailed AChE bound to MuSK to ~50% or less, which suggests that ~50% reduction of the binding affinity is likely to be required to compromise anchoring of ColQ to the NMJ.

Moreover, we demonstrated the pathogenicity of the mutations in a model animal for the first time. We electroporated the three CTD mutations into tibialis anterior muscles of *Colq*$^{-/-}$ mice, and found that each mutation was indeed anchoring-incompetent. To further prove the pathogenicity of one of the mutations in *Colq*$^{-/-}$ mice, we intravenously injected AAV8-*COLQ*-p.Asp447His to *Colq*$^{-/-}$ mice and found that motor deficits remained essentially the same and anchoring of ColQ was not observed at the NMJs.

In vitro plate-binding assays revealed ~50% reduction of binding affinity of ColQ for MuSK for p.Cys444Tyr, p.Asp447His, and p.Arg452Cys (Fig. 3), but these mutants were not at all anchored to the NMJ by in vitro overlay assay (Fig. 2), in vivo electroporation (Fig. 4), and AAV8 treatment (Fig. 5). Among the three mutants, p.Cys444Tyr showed the most preserved binding affinity for MuSK, which, however, was not sufficient to anchor the mutant ColQ to the NMJ in in vitro overlay assay (Fig. 2) and in vivo electroporation (Fig. 4). The presence of heparan sulfate proteoglycans like perlecan at the NMJ in these assays was unlikely to sufficiently compensate for the defective CTD-MuSK interaction, which also underscores a pivotal role of CTD-MuSK interaction on binding of ColQ to the NMJ. Although the same amount of ColQ-tailed AChE was used for in vitro plate-binding and in vitro overlay assays, the amount of MuSK (>150 ng/well) used in in vitro plate-binding assay was likely to be much more than that at the NMJ in in vitro overlay assay, which may account for the difference in up to 50% preservation of ColQ binding in in vitro plate-binding assay and complete lack of ColQ binding in in vitro overlay assay.

Acknowledgments

We thank Yasutaka Ohya, Kumiko Yano, and Koji Nomaru at Division for Research of Laboratory Animals of Nagoya University for technical assistance.

Disclosure statement: The authors declare no conflict of interest.

References

Abicht A, Dusl M, Gallenmuller C, Guergueltcheva V, Schara U, Della Marina A, Wibbeler E, Almaras S, Mihaylova V, von der Hagen M, Huebner A, Chaouch A, et al. 2012. Congenital myasthenic syndromes: achievements and limitations of phenotype-guided gene-after-gene sequencing in diagnostic practice: a study of 680 patients. Hum Mutat 33:1474–1484.

Aihara H, Miyazaki J. 1998. Gene transfer into muscle by electroporation in vivo. Nat Biotechnol 16:867–870.

Arikawa-Hirasawa E, Rossi SG, Rotundo RL, Yamada Y. 2002. Absence of acetylcholinesterase at the neuromuscular junctions of perlecan-null mice. Nat Neurosci 5:119–123.

Cartaud A, Strochlic L, Guerra M, Blanchard B, Lambergeon M, Krejci E, Cartaud J, Legay C. 2004. MuSK is required for anchoring acetylcholinesterase at the neuromuscular junction. J Cell Biol 165:505–515.

Chan SH, Wong VC, Engel AG. 2012. Neuromuscular junction acetylcholinesterase deficiency responsive to albuterol. Pediatr Neurol 47:137–140.

Donger C, Krejci E, Pou Serradell A, Eymard B, Bon S, Nicole S, Chateau D, Gary F, Fardeau M, J. M, Guicheney P. 1998. Mutation in the human acetylcholinesterase-associated collagen gene, *COLQ*, is responsible for congenital myasthenic syndrome with end-plate acetylcholinesterase deficiency (Type Ic). Am J Hum Genet 63:967–975.

Ellman GL, Courtney KD, Andres V, Jr., Feather-Stone RM. 1961. A new and rapid colorimetric determination of acetylcholinesterase activity. Biochem Pharmacol 7:88–95.

Engel AG. 2012. Congenital myasthenic syndromes in 2012. Curr Neurol Neurosci Rep 12:92–101.

Engel AG, Lambert EH, Gomez MR. 1977. A new myasthenic syndrome with end-plate acetylcholinesterase deficiency, small nerve terminals, and reduced acetylcholine release. Ann Neurol 1:315–330.

Engel AG, Ohno K, Sine SM. 2003. Sleuthing molecular targets for neurological diseases at the neuromuscular junction. Nat Rev Neurosci 4:339–352.

Engel AG, Shen XM, Selcen D, Sine SM. 2010. What have we learned from the congenital myasthenic syndromes. J Mol Neurosci 40:143–153.

Feng G, Krejci E, Molgo J, Cunningham JM, Massoulie J, Sanes JR. 1999. Genetic analysis of collagen Q: roles in acetylcholinesterase and butyrylcholinesterase assembly and in synaptic structure and function. J Cell Biol 144:1349–1360.

Ito M, Suzuki Y, Okada T, Fukudome T, Yoshimura T, Masuda A, Takeda S, Krejci E, Ohno K. 2012. Protein-anchoring strategy for delivering acetylcholinesterase to the neuromuscular junction. Mol Ther 20:1384–1392.

Kawakami Y, Ito M, Hirayama M, Sahashi K, Ohkawara B, Masuda A, Nishida H, Mabuchi N, Engel AG, Ohno K. 2011. Anti-MuSK autoantibodies block binding of collagen Q to MuSK. Neurology 77:1819–1826.

Kimbell LM, Ohno K, Engel AG, Rotundo RL. 2004. C-terminal and heparin-binding domains of collagenic tail subunit are both essential for anchoring acetylcholinesterase at the synapse. J Biol Chem 279:10997–11005.

Massoulie J. 2002. The origin of the molecular diversity and functional anchoring of cholinesterases. Neurosignals 11:130–143.

Mihaylova V, Muller JS, Vilchez JJ, Salih MA, Kabiraj MM, D'Amico A, Bertini E, Wolfle J, Schreiner F, Kurlemann G, Rasic VM, Siskova D, et al. 2008. Clinical and molecular genetic findings in COLQ-mutant congenital myasthenic syndromes. Brain 131:747–759.

Muller JS, Petrova S, Kiefer R, Stucka R, Konig C, Baumeister SK, Huebner A, Lochmuller H, Abicht A. 2004. Synaptic congenital myasthenic syndrome in three patients due to a novel missense mutation (T441A) of the COLQ gene. Neuropediatrics 35:183–189.

Ohno K, Brengman J, Tsujino A, Engel AG. 1998. Human endplate acetylcholinesterase deficiency caused by mutations in the collagen-like tail subunit (ColQ) of the asymmetric enzyme. Proc Natl Acad Sci USA 95:9654–9659.

Ohno K, Brengman JM, Felice KJ, Cornblath DR, Engel AG. 1999. Congenital endplate acetylcholinesterase deficiency caused by a nonsense mutation and an A–>G splice-donor-site mutation at position +3 of the collagenlike-tail-subunit gene (COLQ): how does G at position +3 result in aberrant splicing? Am J Hum Genet 65:635–644.

Ohno K, Engel AG, Brengman JM, Shen X-M, Heidenrich FR, Vincent A, Milone M, Tan E, Demirci M, Walsh P, Nakano S, Akiguchi I. 2000. The spectrum of mutations causing endplate acetylcholinesterase deficiency. Ann Neurol 47:162–170.

Rotundo RL, Rossi SG, Anglister L. 1997. Transplantation of quail collagen-tailed acetylcholinesterase molecules onto the frog neuromuscular synapse. J Cell Biol 136:367–374.

Shapira YA, Sadeh ME, Bergtraum MP, Tsujino A, Ohno K, Shen XM, Brengman J, Edwardson S, Matoth I, Engel AG. 2002. Three novel COLQ mutations and variation of phenotypic expressivity due to G240X. Neurology 58:603–609.

Sigoillot SM, Bourgeois F, Lambergeon M, Strochlic L, Legay C. 2010. ColQ controls postsynaptic differentiation at the neuromuscular junction. J Neurosci 30:13–23.

Stem Cell Research (2014) 12, 492–505

Available online at www.sciencedirect.com

ScienceDirect

www.elsevier.com/locate/scr

Perlecan is required for FGF-2 signaling in the neural stem cell niche☆

Aurelien Kerever[a], Frederic Mercier[b], Risa Nonaka[a], Susana de Vega[a], Yuka Oda[a], Bernard Zalc[c,d,e], Yohei Okada[f], Nobutaka Hattori[g], Yoshihiko Yamada[h], Eri Arikawa-Hirasawa[a,g,*]

[a] *Research Institute for Diseases of Old Age, Juntendo University Graduate School of Medicine, Tokyo, Japan*
[b] *Department of Tropical Medicine and Infectious Diseases, John A. Burns School of Medicine, University of Hawaii, Honolulu, HI, USA*
[c] *Université Pierre et Marie Curie-Paris 6, Centre de Recherche de l'Institut du Cerveau et de la Moelle Épinière (CRICM), UMRS 975, Paris, 75013 France*
[d] *Inserm, U 975, Paris, 75013 France*
[e] *CNRS, UMR 7225, Paris, 75013 France*
[f] *Department of Physiology and Kanrinmaru project, Keio University, School of Medicine, Shinjuku-ku, Tokyo, Japan*
[g] *Department of Neurology, Juntendo University School of Medicine, Tokyo, Japan*
[h] *National Institute of Dental and Craniofacial Research, NIH, Bethesda, MD, USA*

Received 10 September 2013; received in revised form 26 November 2013; accepted 21 December 2013

Abstract In the adult subventricular zone (neurogenic niche), neural stem cells double-positive for two markers of subsets of neural stem cells in the adult central nervous system, glial fibrillary acidic protein and CD133, lie in proximity to fractones and to blood vessel basement membranes, which contain the heparan sulfate proteoglycan perlecan. Here, we demonstrate that perlecan deficiency reduces the number of both GFAP/CD133-positive neural stem cells in the subventricular zone and new neurons integrating into the olfactory bulb. We also show that FGF-2 treatment induces the expression of cyclin D2 through the activation of the Akt and Erk1/2 pathways and promotes neurosphere formation in vitro. However, in the absence of perlecan, FGF-2 fails to promote neurosphere formation. These results suggest that perlecan is a component of the neurogenic niche that regulates FGF-2 signaling and acts by promoting neural stem cell self-renewal and neurogenesis.

* Corresponding author at: Juntendo University Graduate School of Medicine, Research Institute for Diseases of Old Age, Building 10, Room 606, 2-1-1 Hongo, Bunkyo-ku, Tokyo 113–8421, Japan. Fax: +81 3 3814 3016.
E-mail address: ehirasaw@juntendo.ac.jp (E. Arikawa-Hirasawa).

1873-5061/$ - see front matter © 2013 The Authors. Published by Elsevier B.V. All rights reserved.
http://dx.doi.org/10.1016/j.scr.2013.12.009

Introduction

In the adult mouse brain, neurogenesis occurs continuously in at least two regions: the subventricular zone (SVZ) of the lateral ventricle (Altman, 1963, 1969; Doetsch et al., 1997) and the subgranular zone of the hippocampal dentate gyrus (Seki and Arai, 1993; Eriksson et al., 1998). In the adult SVZ, subsets of glial fibrillary acidic protein positive ($GFAP^+$) cells (type B cells) function as quiescent neural stem cells (Doetsch et al., 1999), although a portion of these cells are slowly dividing at any given time. These quiescent cells qualify as being activated when they begin to co-express the epidermal growth factor receptor (EGF-R) and come into contact with the ventricle (Pastrana et al., 2009). Then, they give rise to rapidly proliferating cells called "transit-amplifying cells" (type C cells), which stop expressing GFAP but still express EGF-R. The cells then differentiate into doublecortin (DCX)-expressing neuroblasts (type A cells) that migrate along the rostral migratory stream (RMS) towards the olfactory bulb (Lois and Alvarez-Buylla, 1994; Petreanu and Alvarez-Buylla, 2002). They finally integrate into both the granule cell layer (GCL) and glomerular layer (GL) of the olfactory bulb, where they express mature neuronal markers, such as NeuN (Winner et al., 2002).

The early signaling cues promoting the proliferation and differentiation of the neural stem and progenitor cells (NSPCs) are yet to be elucidated. Recent studies have proposed that blood vessels are critical elements of the neurogenic niches in both the hippocampus (Palmer et al., 2000) and the SVZ (Mercier et al., 2002; Shen et al., 2008; Tavazoie et al., 2008). In addition, Mercier et al. (2002) previously characterized basal lamina-like structures, termed fractones, in the vicinity of NSPCs in the adult SVZ. Fractones present extracellular branched fractal structures in direct contact with NSPCs in the adult neurogenic niche, thereby suggesting fractones' role in neurogenesis (Altman, 1963, 1969; Doetsch et al., 1997; Mercier et al., 2002, 2003).

Fractones are composed of different extracellular matrix (ECM) molecules, such as laminin ($\beta1$ and $\gamma1$ but not $\alpha1$), collagen IV, nidogen, and perlecan (Mercier et al., 2002; Kerever et al., 2007). They are able to capture/bind the neurogenic growth factor FGF-2 from the extracellular environment. This trapping of FGF-2 involves binding to heparan sulfate chains (Kerever et al., 2007; Douet et al., 2012). Furthermore, FGF-2 promotes neurogenesis in developing (Raballo et al., 2000; Maric et al., 2007; Pastrana et al., 2009) and adult brains (Lois and Alvarez-Buylla, 1994; Palmer et al., 1995; Petreanu and Alvarez-Buylla, 2002).

We previously showed that perlecan (*HSPG2*), a major heparan sulfate proteoglycan (HSPG) in basement membranes, is present in both blood vessel walls and fractones in the neurogenic niche (Kerever et al., 2007). Perlecan interacts with extracellular molecules, growth factors, and cell surface receptors (Rapraeger, 1995; Winner et al., 2002; Chan et al., 2009), and is implicated in many biological functions in tissue development, homeostasis, and diseases (Arikawa-Hirasawa et al., 1995, 1999; Palmer et al., 2000; Arikawa-Hirasawa et al., 2001, 2002a, 2002b; Xu et al., 2010). Perlecan promotes growth factor receptor binding, such as FGF-2, to stimulate mitogenesis and angiogenesis (Yayon et al., 1991; Aviezer et al., 1994; Mercier et al., 2002; Shen et al., 2008; Tavazoie et al., 2008). A perlecan analog in Drosophila has also been implicated in the reactivation of proliferation in quiescent neural stem cells (NSCs) (Voigt et al., 2002).

Perlecan deficiency causes perinatal lethal chondrodysplasia in mice and in humans (Arikawa-Hirasawa et al., 1999; Costell et al., 1999; Arikawa-Hirasawa et al., 2001), and perlecan knockout ($HSPG2^{-/-}$) mice present impaired indian hedgehog expression and FGF-1 signaling and abnormal cephalic development (Arikawa-Hirasawa et al., 1999). $HSPG2^{-/-}$ mice die at or just before birth due to defects in tracheal cartilage. Furthermore, Giros and colleagues reported a disrupted distribution of sonic hedgehog (Shh) and impaired forebrain development in perlecan-null mice (Girós et al., 2007). We previously created perinatal lethality rescued ($Hspg2^{-/-}$-Tg) mice by expressing recombinant perlecan specifically in the cartilage of the perlecan-null ($HSPG2^{-/-}$) genetic background, in order to study the role of perlecan in tissue homeostasis in adult mice. We used these $HSPG2^{-/-}$-Tg mice to show that perlecan is critical for maintaining fast muscle mass and fiber composition, through regulation of myostatin signaling (Xu et al., 2010).

In the present report, we studied the role of perlecan in the maintenance and fate of NSCs, and in response to FGF-2 stimulation in the SVZ of $Hspg2^{-/-}$-Tg mice. The absence of perlecan resulted in the depletion of $CD133^+$ NSCs. In addition, FGF-2 treatment failed to induce an increase in activation of Akt and Erk1/2 pathways both *in vivo* and *in vitro* in the absence of perlecan. Furthermore, FGF-2 failed to induce cyclin D2 expression and to promote the formation of neurospheres. Taken together, our results indicate that the absence of perlecan is detrimental for $CD133^+$ NSC population and for adult neurogenesis, suggesting that it is a critical component of the adult neurogenic niche.

Materials and methods

Animals

Perlecan-null ($Hspg2^{-/-}$) mice die at birth because of premature cartilage development (Arikawa-Hirasawa et al., 1999). To restore cartilage abnormalities, we used a cartilage-specific Col2a1 promoter/enhancer to generate a perlecan transgenic mouse line (WT-Tg, $Hspg2^{+/+}$; Col2a1-Hspg2Tg/-), which expressed recombinant perlecan in cartilage (Tsumaki et al., 1999). We subsequently created lethality-rescued mice ($Hspg2^{-/-}$-Tg, $Hspg2^{-/-}$; Col2a1-Hspg2Tg/-) by mating the transgenic mice with heterozygous $Hspg2^{+/-}$ mice (Xu et al., 2010). We maintained these mice on the mixed genetic background of C57BL/6 and 129SvJ. In this study, WT-Tg mice (control) and $Hspg2^{-/-}$-Tg (perlecan knockout) mice were used. All animal protocols were approved by the Animal Care and Use Committee of Juntendo University.

BrdU incorporation and FGF-2 treatment assays

Mice that were 8–12 weeks old were used in this study. Nine-week-old mice were sacrificed 48 h after intracerebroventricular (ICV) injection of BrdU (1 μl of 40 mg/ml; WT-Tg, $n = 5$; $Hspg2^{-/-}$-Tg, $n = 5$). Eight-week-old mice received daily intraperitoneal injections of BrdU (50 mg/kg

of body weight) for 5 days. They were sacrificed 4 weeks after the fifth and last injections (WT-Tg, $n = 5$; Hspg2$^{-/-}$-Tg, $n = 5$). For FGF-2 stimulation in NSCs, 9-week-old mice were injected ICV with FGF-2 (1 μl, 0.075 μg/μl). Mice were sacrificed 48 h after ICV injections.

Histology

Mice were deeply anesthetized and perfused transcardially with cold paraformaldehyde (4%) in a 100 mM phosphate buffer, pH 7.4. Brains were dissected, immersed overnight in fixative, and transferred to 30% sucrose for at least 48 h. Brains were frozen and cut into 25 μm coronal sections with a cryostat. For extracellular matrix staining, fresh brains were frozen in isopentane. Sections were stored at −20 °C until staining.

Immunofluorescence

Sections were post-fixed in cold paraformaldehyde for 10 min and washed in PBS. Sections were then placed in a 0.5% Triton X-100/PBS solution for 15 min, followed by 15 min of a blocking solution (0.2% gelatin/PBS). Primary antibodies were applied for either 2 h at room temperature or overnight at 4 °C in blocking solution. The following primary antibody dilutions were used: rat anti-perlecan (1:400, clone A7L6, Chemicon, Temecula, CA), rabbit polyclonal anti-laminin (1:1000, Sigma, St Louis, MO), rabbit polyclonal anti-agrin (1:1000, kind gift of Dr. Sasaki, add his location), mouse anti-heparan sulfate (10E4 epitope, 1:400, Seikagaku Corporation, Tokyo, Japan), mouse anti-heparan sulfate (JM403 epitope, 1:400, Seikagaku Corporation, Tokyo, Japan), mouse anti-delta heparan sulfate (3G10 epitope, 1:400, Seikagaku Corporation, Tokyo, Japan), mouse anti-chondroitin sulfate (CS-56) (1:400, Abcam, Cambridge, MA), rat anti-CD133 (1:50, Chemicon, Temecula, CA), rabbit anti-GFAP (1:400, Dako, Glostrup, Denmark), mouse anti-GFAP conjugated to alexafluor 647 (1:400, Cell Signaling Tech, Boston, MA), rabbit polyclonal anti-EGF-Receptor (1:200, Chemicon, Temecula, CA), goat anti-doublecortin (DCX) (1:200, Santa Cruz Biotechnology, Santa Cruz, USA), mouse anti-NeuN (1:200, Chemicon, Temecula, CA) and rabbit anti-ssDNA (1:200, Immuno-Biological Laboratories Co, Fujioka, Gunma, Japan). Sections were then rinsed, and secondary antibodies were applied for 40 min at room temperature. The following fluorochrome-conjugated secondary antibody dilutions were used: donkey anti-mouse-CY5, donkey anti-goat-FITC (1:400, Jackson ImmunoResearch Laboratories, West Grove, USA), goat anti-rabbit alexafluor-488, and goat anti-mouse-FITC (1:400 Molecular probes, Invitrogen Corporation, Carlsbad, USA). Sections were rinsed in PBS before being treated in 2 N HCl for 30 min at 37 °C and then incubated for 10 min in a 0.1 M borate buffer (pH 8.5). Sections were rinsed before overnight incubation in rat anti-BrdU (1:800, AbD Serotec, MorphoSys AG, Planegg, Germany). Sections were rinsed and then incubated for 1 h with donkey anti-rat-CY3 (1:400, Jackson, ImmunoResearch Laboratories, West Grove, USA). Sections were rinsed and then incubated for 10 min in bis-benzimide (1:3000, Molecular Probes, Invitrogen Corporation, Carlsbad, CA). After extensive washes, sections were mounted in fluoro-gel with tris buffer (Electron Microscopy Sciences, Hatfield, USA).

Flow cytometry analysis

SVZs from 12-week-old WT-Tg and Hspg2$^{-/-}$-Tg mice ($n = 3$) were carefully dissected following the procedure described by Fischer and colleagues (Fischer et al., 2011). SVZs were then cut into small pieces and incubated for 15 min with a papain neural tissue dissociation kit from Miltenyi (Auburn, CA, USA). Cells were mechanically dissociated and passed through a 40 μm cell strainer. After washing in stain buffer (BD Bioscience, San Jose, CA, USA), the cells were incubated for 30 min in 50 μl of stain buffer with anti CD133-PE (1:20, eBioscience, San Diego, CA, USA) and with alexafluor-488-conjugated EGF (1:20, Molecular probes, Eugene, OR, USA). Cells were then fixed and permeabilized (BD Cytofix/Cytoperm kit, BD Biosciences, San Jose, CA, USA) prior to incubation with alexafluor-647 GFAP (1:40, Cell Signaling Technology, Danvers, MA, USA). Cells were washed and resuspended in 500 μl of stain buffer to perform flow cytometry analysis. The analysis was performed using a BD LSR Fortesa cell analyzer with the gate set using an appropriate isotype control.

Neurosphere culture

The cortexes of E16.5 mice were dissected and mechanically dissociated to single cell suspension. Cells were plated for 4 h to allow adherent cells to attach to the plate in DMEM/F12 and B27. Cells in suspension were recovered, counted and placed in 96 well plates at low density (300 cells/well) in 200 μl of DMEM/F12 and B27 containing EGF 20 ng/ml and different concentrations of FGF-2. Conditions were as follows: no FGF-2, control (FGF-2 20 ng/ml), and 10X FGF-2 (FGF-2 200 ng/ml). After one week in culture, the number and the size of neurospheres in each well were assessed. For differentiation, primary neurospheres were cultured for an additional 7 days on collagen-1 coated slide chambers with DMEM/F12 and 10% fetal calf serum prior to fixation in 10% PFA. Differentiated cells were then stained with GFAP, Tuj-1, and O4. Whole neurospheres were fixed in PFA (10 min) prior to immunocytochemistry as described above.

Western blotting

Whole SVZ or neurospheres were lysed in RIPA buffer (0.5% deoxycholate, 0.1% SDS, 250 mM NaCl, 25 mM Tris–HCl, pH 8, Igepal CA630, 5 mM EDTA, protease inhibitor and phosphostop; sonication 3 times 5 s). Lysates were boiled in an LDS-sample buffer (Invitrogen) with DTT for 10 min. The samples were loaded on 4–12% polyacrylamide Bis-Tris gels (Invitrogen). After electrophoresis, the proteins were transferred to a PVDF membrane (Invitrogen). The membrane was blocked with 5% skim milk in Tris-buffered saline-0.1% Tween 20, and incubated with the indicated antibodies. Primary antibodies used in Western blotting were Akt (rabbit polyclonal, Cell signaling), phospho-Akt (mouse IgG, Cell signaling), Erk1/2 (rabbit polyclonal, Cell signaling), phospho-Erk1/2 (rabbit polyclonal, Cell signaling). Secondary

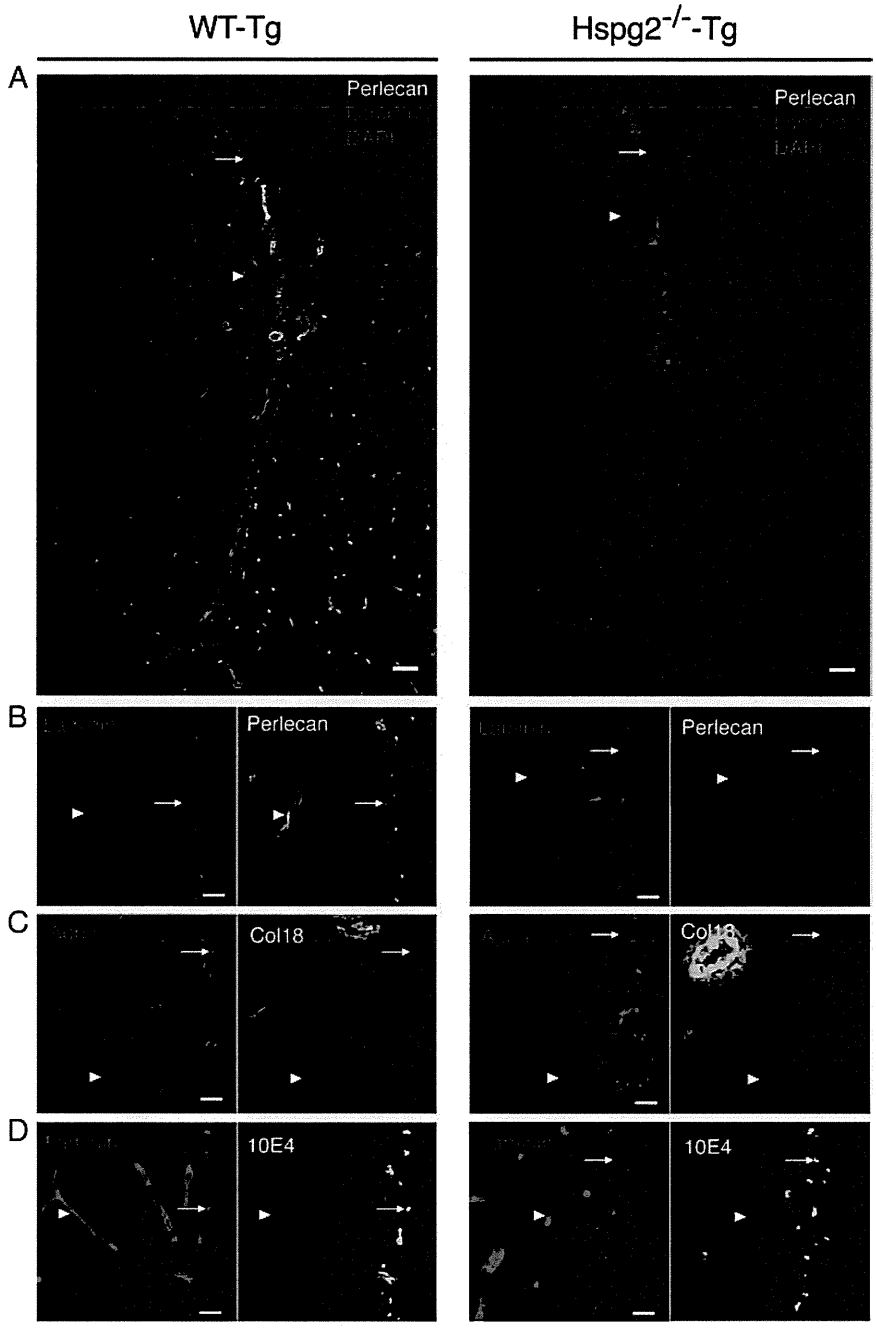

Figure 1 Extracellular matrix content in the SVZ. (A, B) Confocal images of the lateral ventricle of control (WT-Tg) and lethality-rescued perlecan-null mice (Hspg2$^{-/-}$-Tg), showing staining with perlecan (green), laminin-111 (polyclonal, red) and DAPI (blue). Perlecan expression co-localized with laminin on all blood vessels (arrowhead) and fractones (arrow) in the WT-Tg mice, but was absent in the Hspg2$^{-/-}$-Tg. (B, C, D) High magnification of the SVZ. The ependymal wall is on the right of each image and the parenchyma on the left. (C) Agrin (red) display co-localizes with laminin and perlecan while collagen 18 expression (green) is restricted to parenchymal (distance from the ventricle > 50 μm) or large (diameter > 30 μm) blood vessels. Collagen 18 was absent from SVZ capillaries (arrowhead) and from fractones (arrow). (D) The N-sulfated heparan sulfate marker (10E4, green) is strongly present in fractones (arrow) and in SVZ blood vessels (arrowhead), but its expression greatly decreases in the parenchymal blood vessels. Scale bar is 50 mm in A and 20 μm in B, C, and D.

antibodies were rabbit IgG-HRP (Amersham) and mouse IgG-HRP (Amersham). SuperSignal West Dura Chemiluminescent Substrate (Thermo Scientific) was used to detect proteins.

Quantitative real time PCR

RNA from either whole SVZ or neurospheres was extracted using TRIzol reagent (Invitrogen). cDNA was synthetized

using the RT^2 First stand kit from Qiagen. Real time PCR was performed using RT^2 qPCR primer assays and RT^2 SYBR green mastermix from Qiagen on a Fast 7500 Real Time Cycler (Applied Biosystems). Analysis was performed using the web-based application provided by Qiagen.

Quantification and statistical analysis

Analysis was performed using a Leica TCS-SP5 confocal laser scanning microscope. Whole ventricles were reconstructed from pictures taken with 20× plan-apochromat dry objectives (0.7). Serial coronal sections of the SVZ between

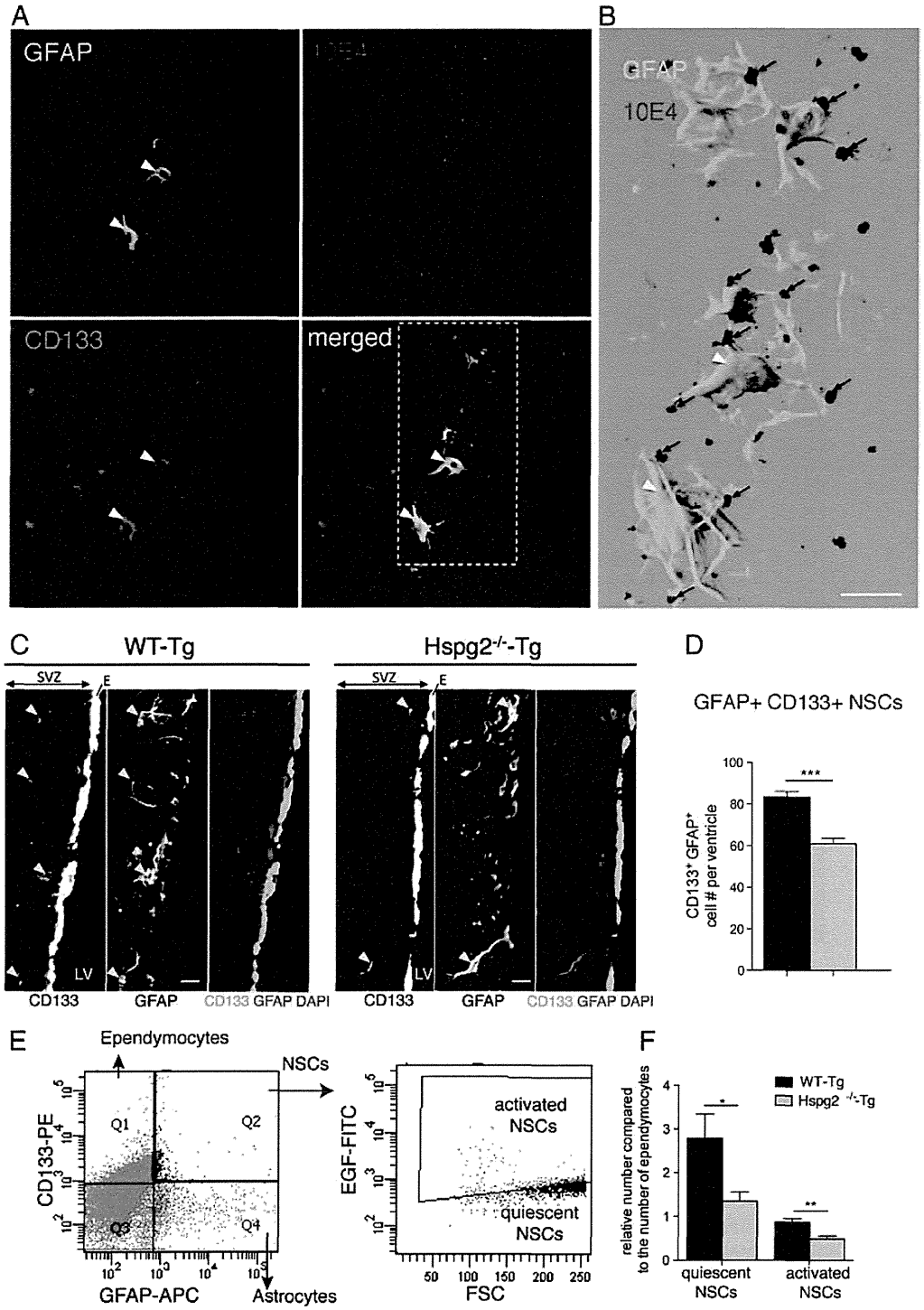

Bregma A 1.1 and Bregma A 0.7 were labeled with either GFAP, CD133, EGF-R, DCX, or BrdU. Cells were counted on images taken from ventricles using ImageJ (ImageJ 1.45 o, Wayne Rasband, NIH, USA). $CD133^+/GFAP^+$ (for type B cells), $EGF\text{-}R^+/GFAP^+$ (for activated type B cells), $EGF\text{-}R^+/GFAP^-$ (for type C cells), and DCX^+ (for type A cells) populations were quantitated by cell type. Serial coronal sections of the RMS between Bregma A 3.2 and Bregma A 3.0 were labeled with DCX, GFAPs, and BrdU. The size of the RMS was assessed by measuring the cluster of DCX^+ cells with ImageJ. Serial coronal sections of the OB between Bregma A 4.3 and Bregma A 4.4 were labeled with NeuN, GFAPs, and BrdU. For neurosphere cultures, statistics were made from 6 wells per condition per animal (from 6 WT-Tg and 4 $Hspg2^{-/-}$-Tg forebrain). Data are presented as the total number of cells per ventricle (mean ± SEM) and analyzed using the Unpaired Student's *t*-test with confidence intervals of 99% or one-way analysis of variance coupled with the Bonferroni post-test (Graph-Pad Prism version 5.0 for Mac OS X, Graph-Pad Software, San Diego, CA).

Results

Perlecan deficiency induces no obvious change in other ECM components in the neurogenic niche

We studied the role of perlecan in NSCs by first comparing the ECM content in the SVZ of $HSPG2^{-/-}$-Tg mice with that of control mice (WT-Tg; Fig. 1). In control mice, perlecan was localized in fractones and all blood vessel basement membranes (SVZ and adjacent neural nuclei). In the $HSPG2^{-/-}$-Tg mice, perlecan was completely absent, but laminin-111 staining, an another basement membrane component which consists of laminin α1 (Lama1), β1 (Lamb1), and γ1 (Lamc1) chains, was still displayed in both fractones and blood vessels (Figs. 1A, B). Next, we investigated other basement membrane heparan sulfate proteoglycans (HSPGs), such as collagen 18 and agrin. While agrin displayed the same patterns as laminin-111 and perlecan, collagen 18 was only expressed in the basement membranes of blood vessels from neural nuclei adjacent to the SVZ and was absent in the fractones and SVZ blood vessel walls of control mice (Fig. 1C).

We also investigated the presence of heparan sulfate (HS) and chondroitin sulfate (CS) chains. Three types of antibodies to heparan sulfate (HS) chains were used: 10E4 (HS epitope including N-sulfated glucosamine) (Fig. 1D), JM403 (HS epitope including N-unsubstituted glucosamine) (Supplemental Fig. 1A), and 3G10 (HS neo-epitope generated by HS chains digestion by heparatinase) (Supplemental Fig. 1B). Immunostaining with these antibodies showed similar localizations of HSs. They were all strongly expressed in fractones and in SVZ blood vessels, but their expression was substantially weaker in blood vessels outside the SVZ of both WT-Tg and $Hspg2^{-/-}$-Tg mice. Antibody CS-56 to CS types A and C did not stain either fractones or most of the SVZ blood vessels, but did stain blood vessels of the neural nuclei adjacent to the SVZ and the pericellular matrix of SVZ cells (Supplemental Fig. 1C). The absence of perlecan did not cause any obvious visible change in the expression of these HS and CS chains in the SVZ. These results suggest that, in the absence of perlecan, basement membranes exist and other HS chain-containing basement membrane components, such as agrin, are present in fractones and in most SVZ blood vessels.

Perlecan presence is critical for neural stem cell maintenance and for neurogenesis in the SVZ

We next investigated the maintenance of NSCs and neurogenesis in the SVZ of $Hspg2^{-/-}$-Tg mice. We characterized the cell identity with several cell type markers, such as GFAP, CD133, EGF-R, and DCX. CD133, also known as Prominin 1 (PROM1), is a marker of cancer stem cells and has been used to identify NSCs in both humans and rodents (Uchida et al., 2000; Corti et al., 2007; Mirzadeh et al., 2008). We used CD133 as a marker for NSCs, in addition to another NSC marker, GFAP. This combination allowed us to distinguish NSCs from $CD133^+$ ependymocytes and $GFAP^+$ astrocytes (Fig. 2A, arrowheads). These NSCs sent many processes in the direction of close-by fractones, thus contacting most fractones in their vicinity (Fig. 2B).

We found a 27% decrease in the number of $CD133^+$ NSCs in $Hspg2^{-/-}$-Tg mice (WT-Tg: 83.55 ± 2.60 $CD133^+/GFAP^+$ cells per ventricle, $Hspg2^{-/-}$-Tg: 61.06 ± 2.60; Figs. 2C,D). This result was confirmed by flow cytometry analysis of the SVZ. Both quiescent ($CD133^+$ $GFAP^+$ $EGF\text{-}R^-$) and activated ($CD133^+$ $GFAP^+$ $EGF\text{-}R^+$) NSCs were significantly reduced in the $Hspg2^{-/-}$-Tg (Figs. 2E,F). The number of activated type B cells was reduced by 53% in the absence of perlecan (WT-Tg: 5.06 ± 0.22 $EGF\text{-}R^+/GFAP^+$ cells per ventricle; $Hspg2^{-/-}$-Tg:

Figure 2 Neural stem cell maintenance in perlecan null mice. (A) Confocal image of the surface of the ependymal wall of the lateral ventricle stained with CD133, GFAP and heparan sulfate chains (10E4) reveals fractones (10E4 staining) in the vicinity of $CD133^+GFAP^+$ NSCs (arrowheads). (B) Shadow projection of a Z-stack of the insert in A (realized with Imaris software) shows NSCs contacting numerous fractones (arrows). (C) Confocal image of the SVZ (striatum side) displaying CD133 and GFAP staining in WT-Tg and $Hspg2^{-/-}$-Tg. CD133 is expressed strongly by ependymocytes and is also present in SVZ NSCs. GFAP is expressed by SVZ astrocytes and NSCs. We discriminated SVZ NSCs by counting positive cells for both CD133 and GFAP in the subependymal layer (arrows show four double positive cells in the image for WT-Tg SVZ and two in the image for $Hspg2^{-/-}$-Tg SVZ. (D) Bar chart displaying the total number $CD133^+GFAP^+$ NSCs per ventricles in WT-Tg and $Hspg2^{-/-}$-Tg. In the $Hspg2^{-/-}$-Tg mice $CD133^+GFAP^+$ NSC number was decreased by 27%. The data are expressed as mean ± SEM (n = 5, *** indicates P-value of $P < 0.0001$; Student's t-test). (E) Dot plot depicting the characterization of NSCs by flow cytometry analysis and the separation of activated NSCs (EGF + fraction) and quiescent NSCs (EGF-fraction). (F) Bar chart displaying the number of quiescent NSCs and activated NSCs (for one hundred ependymocytes CD133+ GFAP-) in WT-Tg and $Hspg2^{-/-}$-Tg SVZ assessed by flow cytometry analysis. Both quiescent and activated NSCs are reduced in the $Hspg2^{-/-}$-Tg brain. The data are expressed as mean ± SEM (n = 3, * indicates P-value of $P = 0.0159$, ** indicates P-value of $P = 0.0069$; Student's t-test). Scale bar: 10 μm. SVZ: subventricular zone; E: ependyma; LV: lateral ventricle.

2.35 ± 0.17; Fig. 3B). The number of type C cells was decreased by 20% (WT-Tg: 37.53 ± 2.01 EGF-R$^+$/GFAP$^-$ cells per ventricle; Hspg2$^{-/-}$-Tg: 29.94 ± 1.14; Fig. 3C).

We also analyzed the neuroblast population (DCX$^+$ cells) and proliferating cells in the SVZ. The number of neuroblasts decreased by 18% in the absence of

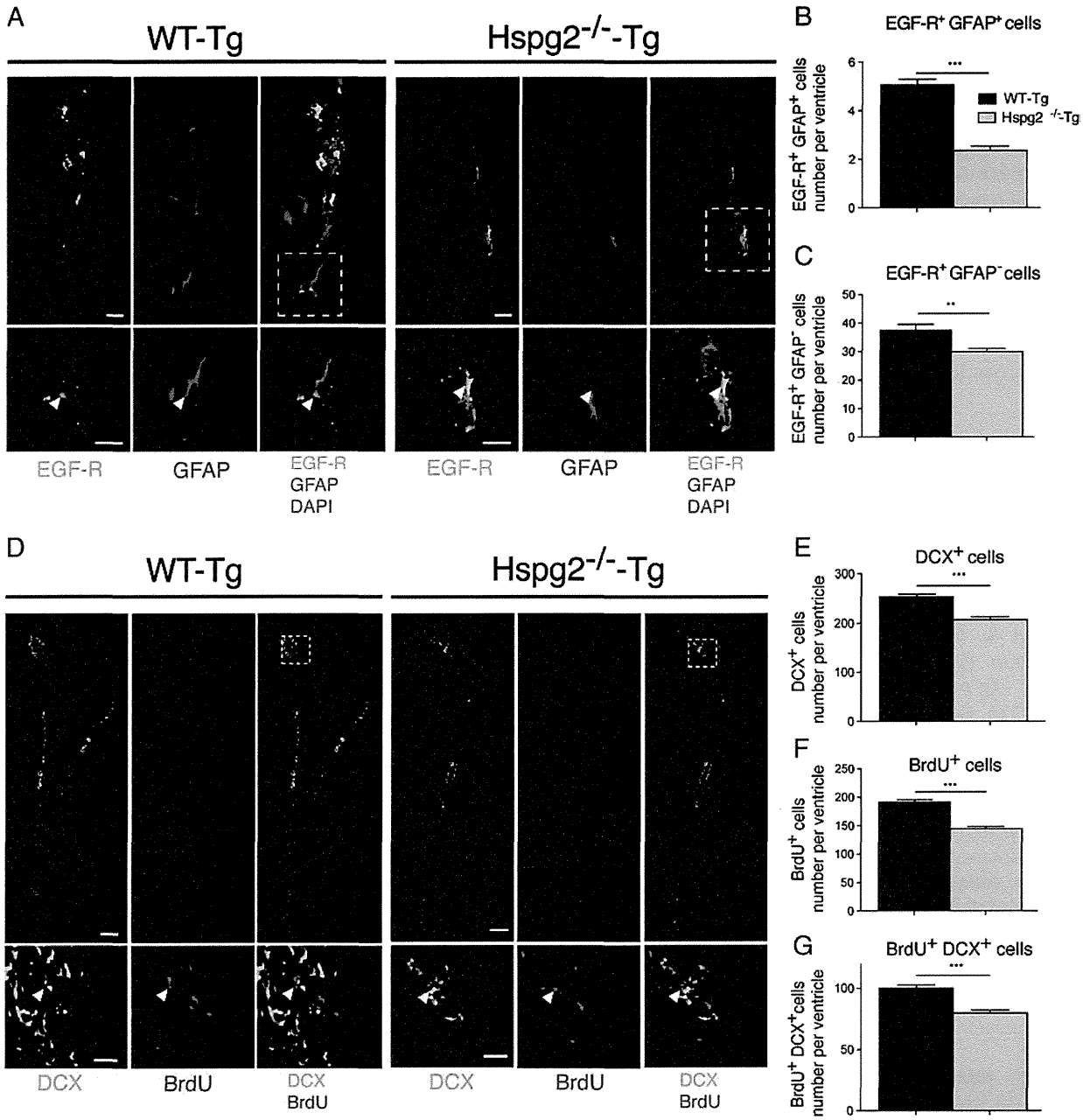

Figure 3 Neurogenesis in the SVZ of perlecan null mice. (A) Confocal image of the SVZ (striatum side) showing EGF-R, GFAP, and DAPI staining in WT-Tg and Hspg2$^{-/-}$-Tg mice. The insert shows examples of double positive EGF-R$^+$GFAP$^+$ (activated type B cells) at a higher magnification (arrowhead). (B) Bar chart indicates the total number of EGF-R$^+$GFAP$^+$ cells (activated type B cells) per ventricle in WT-Tg and Hspg2$^{-/-}$-Tg mice. In the Hspg2$^{-/-}$-Tg mice, EGF-R$^+$GFAP$^+$ cell numbers were decreased by 53%. (C) Bar chart displaying total number EGF-R-GFAP$^+$ cells (type C cells) per ventricle in WT-Tg and Hspg2$^{-/-}$-Tg mice. In the Hspg2$^{-/-}$-Tg mice, EGF-R$^+$GFAP$^+$ cell numbers were decreased by 20%. (D) Reconstructed lateral ventricle from a confocal image displaying DCX and BrdU staining. Insert shows the horn of the lateral ventricle at a higher magnification. Arrowhead shows a double-positive DCX$^+$BrdU$^+$ cell. (E, F, G) Bar chart indicates the total number of DCX$^+$ cells (type A cells, E), BrdU$^+$ cells (proliferating cells), and DCX$^+$BrdU$^+$ cells (newly born type A cells) per ventricle in WT-Tg and Hspg2$^{-/-}$-Tg mice. In the Hspg2$^{-/-}$-Tg mice, DCX$^+$ cell numbers decreased by 18%, proliferating cell numbers decreased by 25%, and newly formed type A cell numbers decreased by 20%. The data are expressed as mean ± SEM (n = 5, *** indicates P-value of $P < 0.0001$; ** indicates P-value of $P < 0.01$; Student's t-test). Scale bar: 10 μm in A, 100 μm in D and 30 μm in insert in D.

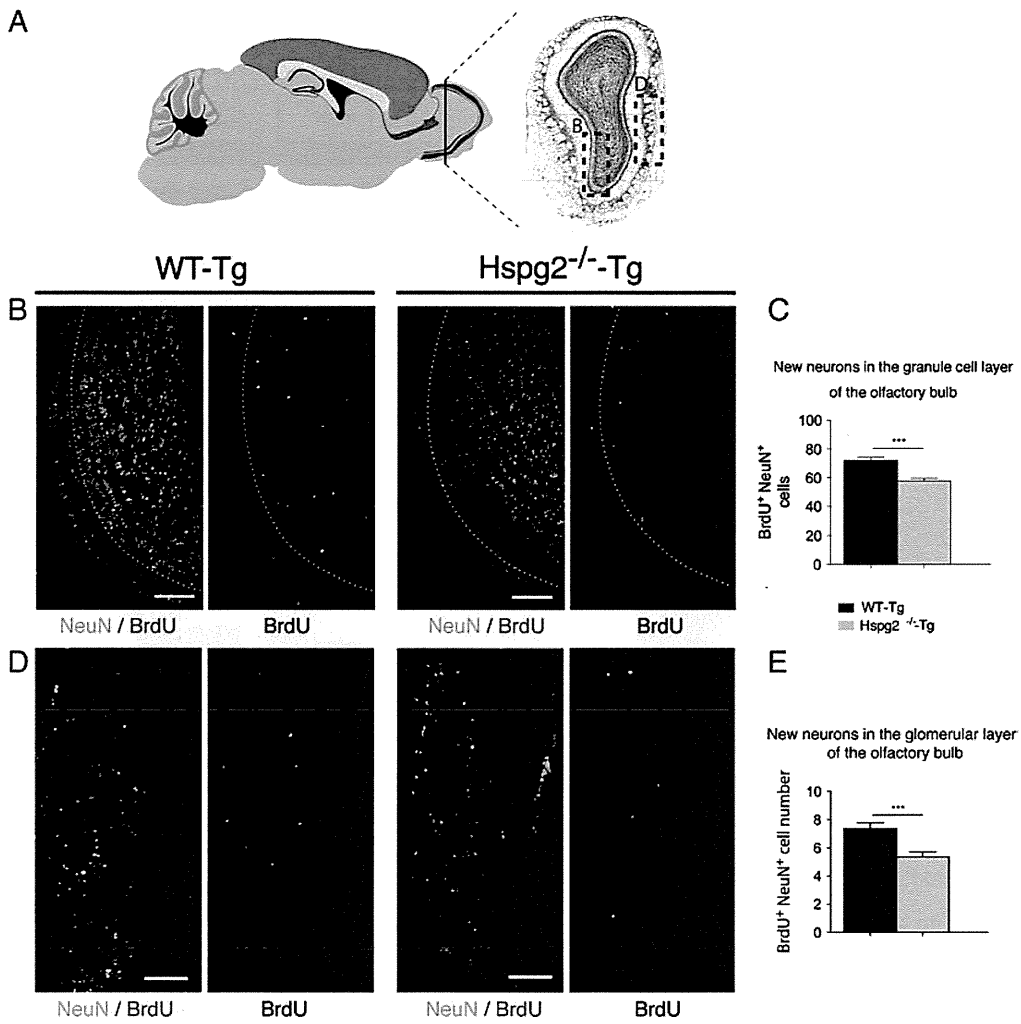

Figure 4 New neurons in the olfactory bulb in perlecan null mice. (A) Drawing of a sagittal section of a mouse brain showing the localization of the coronal section (Nissl staining showing the lateral ventricle at bregma A +4). Insert depicts the area where confocal images in Fig. 5B and D were taken. (B) Confocal image of the granule cell layer (GCL) of the OB displaying NeuN and BrdU staining in WT-Tg and Hspg2$^{-/-}$-Tg mice. Dotted lines show the boundary of the GCL. Overall, 95% of BrdU$^+$ cells co-localized with the mature neuronal marker NeuN. (C) Bar chart indicates the total number of BrdU$^+$NeuN$^+$ cells (new neurons) in one field (0.624 μm^2) of the GCL (5B represent half of a field). The number of proliferating cells in the GCL decreased by 20% in Hspg2$^{-/-}$-Tg mice. (D) Confocal image of the glomerular layer (GL) of the OB indicates NeuN and BrdU staining in WT-Tg and Hspg2$^{-/-}$-Tg mice. (E) Bar chart indicates the total number of BrdU$^+$NeuN$^+$ cells (new neurons) in one field (0.312 μm^2 as shown in 5D) of the GL. The number of proliferating cells in the GL decreased by 27% in Hspg2$^{-/-}$-Tg mice. The data are expressed as means ± SEM (n = 5, *** indicates P-value of $P < 0.0001$; Student's t-test).

perlecan (WT-Tg: 253.80 ± 5.52 DCX$^+$ cells per ventricle; Hspg2$^{-/-}$-Tg: 207.3 ± 6.04; Fig. 3E). To detect newly formed neuroblasts, we analyzed BrdU-positive cells in the SVZ 48 h after a single BrdU injection into the animals. We found that the number of proliferating BrdU$^+$ cells decreased by 25% (WT-Tg: 191.8 ± 4.09 BrdU$^+$ cells per ventricle; Hspg2$^{-/-}$-Tg: 144.6 ± 3.92; Fig. 3F). The number of newly formed neuroblasts (DCX$^+$/BrdU$^+$) also decreased by 20% in the absence of perlecan (WT-Tg: 100.30 ± 2.54 DCX$^+$ cells per ventricle; Hspg2$^{-/-}$-Tg: 79.79 ± 2.45; Fig. 3G). These results indicate that the NSC population was reduced in the perlecan-deficient SVZ, which ultimately resulted in a decrease in neurogenesis.

Fewer new neurons integrate into the olfactory bulb in the Hspg2$^{-/-}$-Tg mice

After exiting the SVZ, neuroblasts migrate toward the olfactory bulb in the rostral migratory stream (RMS). Thus, we followed the fate of the generated neuroblasts 4 weeks after BrdU injection. We found that the RMS size was reduced by 25% in the absence of perlecan (Supplemental Fig. 2 B, C), in accordance with the lower number of neuroblasts generated in the SVZ. Moreover, the majority of BrdU$^+$ cells already exited the RMS and stopped expressing DCX. These cells were detected in the granule cell layer (GCL) adjacent to the RMS (Supplemental Fig. 2D). The numbers of BrdU + cells